Bioactive Materials 6 (2021) 1711–1726

Contents lists available at ScienceDirect

Bioactive Materials

journal homepage: www.sciencedirect.com/journal/bioactive-materials

3D bioprinting of a biomimetic meniscal scaffold for application in tissue engineering

Zhou Jian [a,b,c,1], Tian Zhuang [a,b,c,1], Tian Qinyu [a,b,d], Peng Liqing [a,b], Li Kun [a,b], Luo Xujiang [a,b], Wang Diaodiao [c], Yang Zhen [a,b], Jiang Shuangpeng [a,b], Sui Xiang [a,b], Huang Jingxiang [a,b], Liu Shuyun [a,b], Hao Libo [a,b], Tang Peifu [a,b,***], Yao Qi [c,**], Guo Quanyi [a,b,*]

[a] Medical School of Chinese PLA, Beijing, 100853, China
[b] Institute of Orthopedics, The First Medical Centre, Chinese PLA General Hospital, Beijing, 100853, China
[c] Department of Joint Surgery, Peking University Ninth School of Clinical Medicine, Beijing Shijitan Hospital, Capital Medical University, Beijing, 100038, China
[d] School of Clinical Medicine, Southwest Medical University, Luzhou, Sichuan, 646000, China

ARTICLE INFO

Keywords:
3D bioprinting
Tissue engineering
Meniscus
Scaffold

ABSTRACT

Appropriate biomimetic scaffolds created via 3D bioprinting are promising methods for treating damaged menisci. However, given the unique anatomical structure and complex stress environment of the meniscus, many studies have adopted various techniques to take full advantage of different materials, such as the printing combined with infusion, or electrospining, to chase the biomimetic meniscus, which makes the process complicated to some extent. Some researchers have tried to tackle the challenges only by 3D biopringting, while its alternative materials and models have been constrained. In this study, based on a multilayer biomimetic strategy, we optimized the preparation of meniscus-derived bioink, gelatin methacrylate (GelMA)/meniscal extracellular matrix (MECM), to take printability and cytocompatibility into account together. Subsequently, a customized 3D bioprinting system featuring a dual nozzle + multitemperature printing was used to integrate the advantages of polycaprolactone (PCL) and meniscal fibrocartilage chondrocytes (MFCs)-laden GelMA/MECM bioink to complete the biomimetic meniscal scaffold, which had the best biomimetic features in terms of morphology and components. Furthermore, cell viability, mechanics, biodegradation and tissue formation in vivo were performed to ensure that the scaffold had sufficient feasibility and functionality, thereby providing a reliable basis for its application in tissue engineering.

1. Introduction

The meniscus is a wedge-shaped fibrocartilage tissue that plays an important role during the movement of the knee joint. It is shaped with high edges and a low center, thus allowing it to be perfectly embedded between the femoral condyle and the tibial plateau. However, because of its unique shape, the meniscus is subjected to complex stress environment, including axial, hoop and compressive load [1]. Lesions in the meniscus are frequent clinical sports injuries. Currently, for severe meniscus injury, resection [2] or allogeneic meniscus transplantation [3,4] can be performed, but achieving good outcomes with these techniques, especially in the long term, is difficult for various reasons. The emergence of regenerative repair via tissue engineering has provided promising treatment methods.

Ideal tissue-engineered scaffolds are supposed to closely simulate native tissues so that they can functionally replace the meniscus within a short period of time, delay the progress of osteoarthritis, and promote the regeneration and repair of defective tissues. Various different tissue engineering techniques have been studied for biomimetic applications, such as a silk-collagen scaffold by lyophilization [5], polylactic acid (PLA) electrospun scaffolds with human meniscus cells embedded in extracellular matrix (ECM) hydrogels [6], injectable BMSCs-laden ECM

* Corresponding author. Institute of Orthopedics, the First Medical Centre, Chinese PLA General Hospital, Beijing, 100853, PR China.
** Corresponding author. Department of Joint Surgery, Peking University Ninth School of Clinical Medicine, Beijing Shijitan Hospital, Capital Medical University, Beijing, 100038, China.
*** Corresponding author. Institute of Orthopedics, the First Medical Centre, Chinese PLA General Hospital, Beijing, 100853, China.
E-mail addresses: pftang301@163.com (T. Peifu), yqjh2010@163.com (Y. Qi), doctorguo_301@163.com (G. Quanyi).
[1] Both authors contribute equally to this work.

https://doi.org/10.1016/j.bioactmat.2020.11.027
Received 13 October 2020; Received in revised form 13 November 2020; Accepted 19 November 2020

hydrogels [7] and so on. At different perspectives, all of these scaffolds have verified their effcet on specific meniscal models. However, it is difficult for them to meet the requirements of complex and personalized shapes and properties in clinical patients. The development of three-dimensional (3D) bioprinting offers effective approaches for achieving improved biomimetic strategies.

3D bioprinting is a novel printing technology for biomedical products that uses computer-aided design and manufacturing techniques to precisely print a variety of biological materials via layer-by-layer deposition. This method can rapidly achieve high-precision and personalized printing without the assistance of a mold. Thus far, researchers have explored the 3D bioprinting of biomimetic menisci from different angles and printed synthetic materials with good mechanical properties [8], such as polycaprolactone (PCL), to pursue morphological and mechanical biomimetics, which makes it difficult to provide a good microenvironment for tissue regeneration. Some scholars have tried to improve it by immersing synthetic scaffolds into natural material [9–12], yet the process is relatively complicated and the biological materials cannot be assigned to a particular location. Furthermore, other researchers have fabricated the PCL supporting scaffolds for cell-laden hydrogel encapsulating poly(lactic-co-glycolic acid) (PLGA) microparticles carrying TGF-3 or CTGF in different regions to induce anisotropic phenotypes [13]; however, the study has not focused on the components, compressive modulus or necessary space required for the exchange of substances. Therefore, the better solutions to these problems remain to be found.

Based on the above studies, this study designed a meniscus-derived bioink with printability and cytocompatibility and a customized biomimetic meniscal printing system, i.e., a dual-nozzle + multi-temperature printing system, to integrate the advantages of PCL with that of the cell-laden bioink. One nozzle prints PCL by high-temperature melt deposition to construct a meniscal frame, thereby achieving morphological and mechanical biomimetics, and the other nozzle prints meniscus-derived bioink that consists of gelatin-methacryloyl (GelMA) + meniscal extracellular matrix (MECM) + meniscal fibrocartilage chondrocytes (MFCs), at a fixed temperature to realize componential and microenvironmental biomimetics. In addition, this study also carried out a series of experiments on cell viability, mechanics, biodegradation, and tissue formation in vivo to ensure sufficient feasibility and functionality of the scaffold, thus providing a reliable basis for its subsequent application in tissue engineering.

2. Materials and methods

2.1. Materials

The following materials and tools were used in this study: GelMA (SunP Biotech, Beijing, China); MECM (Institute of Orthopedics, General Hospital of Chinese PLA); MFCs (Institute of Orthopedics, General Hospital of Chinese PLA); pepsin (Sigma-Aldrich, St. Louis, USA); Live/Dead Viability/Cytotoxicity Kit (BioVision, San Francisco, UAS); fetal bovine serum (FBS, GEMINI, USA); Dulbecco's Modified Eagle's Medium/Nutrient Mixture F-12 Ham (DMEM/F12, Corning, USA); penicillin-streptomycin (Thermo Fisher, Waltham, USA); phosphate-buffered saline (PBS, Cellgro, USA); collagenase from *Clostridium histolyticum* (Sigma-Aldrich, St. Louis, USA); trypsin from the bovine pancreas (Sigma-Aldrich, St. Louis, USA); collagen I alpha 1 antibody (Novus Biologicals, USA); 3D Bioprinter (SunP Biotech, Beijing, China); TCS-SP8 laser scanning confocal microscope (Leica, Wetzlar, Germany); Q125 sonicator (Qsonica, USA); LS 13 320 laser particle size analyzer (Beckman Coulter, USA); EZ-LX single-stranded electronic universal testing machine (Shimadzu, Japan); 1525 high-performance liquid chromatography system (Waters, USA); micro-computed tomography (CT) system (GE Healthcare, USA); S-4800 scanning electron microscope (Hitachi, Tokyo, Japan); IVIS Spectrum in vivo imaging system (PerkinElmer, USA); CO_2 incubator (Heraeus, Hanau, Germany); and Nano Indenter G200 (Agilent, USA).

2.2. Preparation and characterization of the printable MECM

2.2.1. Preparation characterization of the printable MECM

Decellularized MECM was prepared by wet differential centrifugation from fresh porcine meniscal tissue [14]. The MECM components were verified in a previous study [15]. According to the processing method, the prepared MECM was divided into three groups: the raw group, the pepsin digestion group and the ultrasonic treatment group. MECM was treated with pepsin as previously reported [16]. The ultrasonic treatment was as follows: a Q125 Sonicator (Qsonica, USA) was used to crush the material in an ice trough at an amplitude of 70% and cycle times of 5 s for the pulse and 5 s for the interval.

2.2.2. Analysis of particle size

An LS 13 320 laser particle size analyzer (Beckman Coulter, USA) was used to analyze the particle size distribution of the material. The experiment consisted of two parts. First, the effect of ultrasound time on the MECM suspension was examined, and the suspension was divided into 4 groups according to the ultrasonication time (30 s, 60 s, 90 s and 180 s). Second, the effects of the different treatment methods on the MECM suspension were studied by dividing the samples into the raw group, the pepsin digestion group and the ultrasonic treatment group. The parameters of the test were as follows: The universal liquid module was used for the analysis of particles ranging in size from 0.04 μm to 2000 μm in size at a sample shading rate of 2% and a pump speed of 58%.

2.2.3. Scanning electron microscopy (SEM)

The samples were smeared on a cover glass, air-dried, and coated twice with palladium-platinum alloy at 40 mA. Then, the size and morphology of samples were observed using an S-4800 scanning electron microscope (Hitachi, Tokyo, Japan) in terms of size and morphology.

2.2.4. Quantitative analysis of collagen

A quantitative analysis of the total collagen was performed using a hydroxyproline assay kit (Nanjing Jiancheng Bioengineering, China) according to the kit instructions. Briefly, 200 μl samples were evenly coated on a cover glass and air-dried, and then they were subjected to type I collagen immunofluorescence staining (for details regarding the experimental procedures, refer to the instructions).

2.3. Preparation and characterization of meniscus-derived bioink

2.3.1. Preparation of meniscus-derived bioink and cell encapsulation

Dry GelMA powder was prepared into a 20% (w/v) solution with PBS and then placed in a water bath at 80 °C for 1 h to ensure complete dissolution. Then, 3% MECM (w/v) suspension and lithium phenyl-2,4,6-trimethylbenzoylphosphinate (LAP) were added [17], and the bioink was mixed with PBS to a fixed concentration of 10% GelMA + 0.5% MECM + 0.25% LAP. Finally, we used the bioink to resuspend MFCs. Notably, to ensure cell viability during the long printing process, MFCs-laden bioink needs to be prepared with DMEM/F12 solution containing 20% FBS. Through the above steps, the meniscus-derived bioink, consisting of GelMA (10%, w/v), MECM (0.5%, w/v), LAP (0.25%, w/v), and MFCs (1×10^6/mL), was prepared. Crosslinking was achieved with blue light (405 nm) at an intensity of 90 mW/cm^2 and a duration of 10 s.

MFCs were obtained from New Zealand white rabbits at an age of one month. Isolation and culturing were performed as previously reported [18,19]. When cells reached 80%–90% confluence, they were passaged with 0.25% trypsin digestion. All cells used were P2–P5.

2.3.2. CCK-8 assay

To perform the CCK-8 assay (Dojindo Molecular Technologies, Kumamoto, Japan), 2×10^3 MFCs were cultured in the 96-well plates followed by the immersion of hydrogels in media for 1, 3, 5, and 7 days. After washing with PBS, the MFCs were treated with Dulbecco's modified Eagle's medium (DMEM, 90 μL) and CCK-8 (10 μL) reagent for 2 h. The optical density at 450 nm was analyzed using an Epoch™ Multi-Volume Spectrometer system (BioTek, USA).

2.3.3. Gene expression analysis through RT-PCR

After culturing the samples for 14days, the total RNA of cells was isolated using TRIzol reagent (Tiangen Biotech, China) based on the manufacturer's protocol. The RNA concentration was measured using a NanoDrop system (Thermo Scientifific, USA). Reverse transcription was performed with a cDNA synthesis kit (Thermo Scientifific, USA) following the manufacturer's instructions. Gene expression was analyzed quantitatively with a SYBR-green using 7500 Real-Time PCR system (Applied Biosystems, Life Technologies, USA). The primers and probes for collagen type II (COL2A1), collagen type I (COL1A2), SOX9, and GAPDH were designed based on published gene sequences (NCBI and PubMed). GAPDH was choosen as an endogenous control for our study. The expression levels for each gene were normalized with GAPDH and analyzed using the $\mathbf{2^{-\triangle\triangle CT}}$ method. Each group had three samples.

2.3.4. Cell skeleton and immunofluorescence

The samples were cultured for the specific time, and then fixation, permeabilization and blocking were performed followed by incubation with primary antibodies (1:500) (Novus, USA) and rhodamine-phalloidin (1:200) (Cytoskeleton, USA) for overnight at 37 °C, and with secondary antibodies (1:200) (ZSGB-BIO, China) for 1 h at room temperature. Nuclei were counter stained with DAPI for 15 min and imaged using a confocal microscope.

2.4. Rheological characterization of meniscus-derived bioink

The rheological properties of the bioink were tested by an MCR 301 Advanced Rotational Rheometer (Anton Paar, Austria) using plates with a parallel geometry and a sandblasted (PP25). To prevent the bioink from drying out, the exterior was sealed with paraffin oil. The gelation kinetics of the bioink were measured in the range of 15 °C–37 °C, and the viscoelasticity is expressed by the loss modulus (G″) and the storage modulus (G'). The temperature increased by 1 °C per minute, the strain was 2%, and the frequency was 1 Hz. The temperature-sensitive hysteresis of the bioink was measured at different temperatures. The temperature was rapidly reduced from 37 °C to a predetermined temperature and maintained for 30 min, and the change in viscoelasticity was tested. The viscosity of the bioink was measured at a shear rate ranging from 10^0 to 10^3, and a dynamic frequency sweep was performed at an angular frequency ranging from 10^0 to 10^2. Based on the rheological properties of the bioink, the printability of the bioink was measured according to the spreading ratio. The inner diameter of the nozzle was 200 μm. Four positions were randomly selected to measure the wire diameter (spreading ratio = wire diameter/nozzle inner diameter).

2.5. Printing of the primary model and biomimetic meniscal model

The printing of the primary model included three procedures: (a) 3D printing of the hydrogel with MFCs ("GelMA/MECM" hydrogel, abbreviated as "hydrogel" in subsequent experiments) by the low-temperature nozzle; (b) 3D printing of the PCL scaffold by the high-temperature nozzle; and (c) 3D printing of the primary square models (PCL+ hydrogel+ MFCs) by the dual nozzles. The above printing process was completed using a 3D bioprinter (SunP Biotech, Beijing, China), and the printing parameters are shown in Table 1. The printing of the meniscal model consisted of the following steps: (a) the sheep meniscus was scanned by micro-CT (GE Healthcare, USA) to obtain DCM files. (b) the DCM files were input into Mimics software (version 21.0, Materialise, Belgium) for 3D modeling to generate STL files; (c) the modeling files (.stl) were input into the printer equipped with the software (Biomaker) for planning the printing path in G-code files (Supplementary Fig. 1); (d) the printing parameters were set (Table 1); and (e) printing began. Two nozzles and a triple temperature control system were used for printing. On the printing platform at 20 °C, one nozzle was used to fuse-deposit PCL at 85 °C, and the other nozzle was used to extrude MFC-laden bioink at 20 °C. Additionally, before printing, PCL was supposed to melted adequately in advance to make the printing process smooth. Each layer was printed with 5 s of blue light crosslinking and 5 s of final crosslinking of the whole meniscal scaffold.

Table 1
Parameters for printing the biomimetic meniscal scaffold.

Project	Parameter
3D Bioprinter	
Model	Biomaker
Design software	Biomaker
Printing system	Dual-nozzle + Multitemperature printing system
Power drive	Stepping motor
Printing nozzle	
Type	
Nozzle 1 (PCL)	High-precision dispensing nozzle (400 μm in inner diameter)
Nozzle 2 (hydrogel)	TT nozzle (500 μm in inner diameter)
Moving speed	
Nozzle 1	5 mm/s
Nozzle 2	5 mm/s
Temperature	
Nozzle 1	85 °C
Nozzle 2	20 °C
Printing approach	
Filling	Cross mesh
Curing	Blue light crosslinking (405 nm)
Strand spacing (center to center)	1.5 mm
Printing platform temperature	20 °C

2.6. SEM

The samples were frozen at −80 °C for 12 h and lyophilized for 48 h. The samples were sprayed with a palladium-platinum alloy twice at 40 mA for 40 s each time before the samples were loaded. A S-4800 scanning electron microscope (Hitachi, Tokyo, Japan) was used to observe the details of the scaffold.

2.7. Cell viability

A Live Death@ Viability/Cytotoxicity Kit (BioVision, San Francisco, America) was used to assess the viability of cells in the constructs. According to the printing technique, two experimental groups were formed: the single-nozzle group (hydrogel+ MFCs) and the double-nozzle group (PCL+ hydrogel+ MFCs) to assess the impact of these two printing techniques on cell viability. The printed constructs were cultured for 1 day and 14 days, which was followed by live-dead staining performed according to the reagent instructions. Because the constructs were relatively thick, the staining and cleaning times were appropriately extended. Then, we used a TCS-SP8 laser confocal microscope (Leica, Wetzlar, Germany) to image at 488 and 552 nm, and three randomly selected visual fields were used to quantify the cell viability with Image J (version 1.5.0, NIH).

2.8. Biomechanical analysis

A biomechanical analysis was performed to evaluate the effects of the dual-nozzle printing techniques on the scaffold by an EZ-LX single-

stranded electronic universal testing machine (Shimadzu, Japan). The samples were divided into the PCL + hydrogel group and the PCL group. The strain was set to 10% to simulate the physiological load in humans [20]. At room temperature, a cylindrical model (D = 5 mm, H = 2.5 mm) was used to perform a compression test at a compression rate of 1 mm/min. The sample was also allowed to rebound at a recovery rate of 1 mm/min. With reference to the radial strain (5%) of the physiological meniscus [21], the tensile model (L = 6 mm, W = 6 mm, H = 2.5 mm) was stretched at a rate of 3 mm/min at room temperature. All experiments were performed three times. Young's modulus was calculated from the linear portion after the toe region of the stress-strain curve.

2.9. Subcutaneous degradation

The degradation of hydrogels in vivo was investigated by measuring the fluorescence intensity of Cy7-labeled specimens subcutaneously implanted in mice (Kunming) using an IVIS Spectrum in vivo imaging system. The fluorescent dye Cy7 and bovine serum albumin (BSA) were mixed (referring to the instructions), and then the Cy7-bound BSA was mixed into the bioink for 3D printing. The printed model (L = 5 mm, W = 5 mm, four layers) was placed under the skin of mice in the GelMA, GelMA+MECM and PCL+GelMA+MECM groups, with four mice in each group. At the same time, in the PBS control group, while the same model was placed in PBS and cultured at 37 °C in an incubator out of light. Observations were performed once a week, and the test was terminated when the fluorescence disappeared in more than half of the specimens. The parameters of the IVIS Spectrum in vivo imaging system were as follows: excitation wavelength, 675 nm; emission wavelength, 760 nm; exposure time, 3 s; and binning factor, 8. ImageJ was used to quantify the fluorescence intensity.

2.10. Degradation in situ

A partial defect model in the sheep meniscus was designed to test the stability of the scaffold and whether the rates of tissue regeneration and scaffold degradation match. The experiment was carried out under a scheme approved by the Animal Ethics Committee of the PLA General Hospital, and the experimental animals were purchased from the Experimental Animal Center of the PLA General Hospital.

2.10.1. Surgical procedure

Two sheep weighing approximately 35 kg were included in the PCL group and the PCL + hydrogel group, with 6 samples in each group. The experiment was divided into two time points of 3 months and 6 months. The skin, subcutaneous tissue, and joint capsule were incised to expose the joint cavity and dislocate the patella. Two apertures were drilled in the anterior horn of the medial meniscus (d = 5 mm) with a corneal trephine (Supplementary Fig. 2), and one aperture was drilled in the anterior horn of the lateral meniscus (d = 5 mm). After the scaffolds were implanted and sutured, the joint capsule, subcutaneous tissue, and skin were sutured closed layer by layer. The incision was disinfected, and the animal was allowed to move freely. At the scheduled times, the animals were euthanized, and then material was collected for subsequent evaluation.

2.10.2. Gross evaluation of implants

The fully exposed femoral condyles and the tibial plateau were photographed, and the implants were scored [22]. Three researchers who were blinded to the experimental groups evaluated the menisci using the Gross Evaluation of Meniscus Implant Score (1–3), which was performed according to a previous report [8,23].

2.10.3. Nanoindentation and hardness test

A nanoindenter (G200, Agilent, California, USA) with a Berkovich triangular tip was used to test the mechanical properties of the samples. Each sample was cold-set with epoxy resin and polished to prevent inaccurate data due to an uneven surface. The processed sample was fixed on the test bench, and the continuous stiffness mode was selected. The depth of indentation was 1 μm, and Poisson's ratio was 0.4. Each sample was tested at five points. The data were processed and analyzed with GraphPad Prism (version 8.0, GraphPad Software, Inc.).

2.10.4. Gel permeation chromatography (GPC) test

Variations in the molecular weight of PCL were measured by GPC. The trial was performed with a Waters 1525 high-performance liquid chromatograph, and the detector was a Waters 1424 instrument. The sample (5 mg) was fully dissolved in tetrahydrofuran (THF) as the mobile phase that was degassed under reduced pressure using ultrasound. A syringe was used to draw 100 μL of the mobile phase and evenly inject it into the injector for testing. The flow velocity was set at 1 mL/min, and the temperature was 35 °C.

2.11. Tissue formation in vivo

This experiment was performed under a protocol approved by the Animal Ethics Committee of the PLA General Hospital. The samples were divided into three groups: the PCL group, the PCL+hydrogel group and the PCL+hydrogel+MFCs group, with 8 specimens in each group divided into two time points, i.e., 4 and 8 weeks. The scaffold samples (L: 5 mm, W: 5 mm, H: 2.5 mm) was subcutaneously implanted into female nude mice (18–20 g), and the mice were sacrificed at the predetermined time points. Frozen sections (thickness: 10 μm) of the implants were stained with picrosirius red (PR) and toluidine blue (TB) and subjected to type I collagen immunohistochemistry to assess meniscal tissue formation.

2.12. Statistical analysis

All data are expressed as $\bar{x} \pm s$ and were analyzed with SPSS statistical software (version 22.0, IBM, USA). A comparison of the data among three groups was performed using one-way analysis of variance. A comparison of the data between two groups was performed via a *t*-test. $P < 0.05$ was considered statistically significant.

3. Results

3.1. Characterization of printable MECM

Printing of the biomimetic meniscal scaffold was a complicated process (Fig. 1). It is essential to prepare a meniscus-derived bioink with printability. According to our study, for the bioink, more than 95% of the particles less than 200 μm in diameter could be printed through the nozzle smoothly. The results of the particle size analysis showed that the particle size of the raw MECM was very large, with 76.88% of particles larger than 200 μm, and more than 20% larger than 1000 μm (Fig. 2b and c); as such, these particles did not meet the printing requirements. Consequently, we applied ultrasound to improve the printability. With other parameters remaining the same, the effect of the ultrasonication time on the particle size was investigated first. The results show that the particle size gradually decreased with increasing ultrasonication time. After 30 s and 60 s of ultrasonication, 45.97% and 37.32% of the particles exceeded 200 μm in size, respectively. After 90 s of ultrasonication, 95.50% of the particles were less than 200 μm in size, and after 180 s of ultrasonication, all particles were less than 100 μm in size (Fig 2a, c), which is beneficial for printing a higher-resolution scaffold. To avoid excessive damage to the original ingredients and to ensure printability, 90 s of ultrasonication was selected for subsequent research. In addition, a particle size analysis was performed in combination with the approach of pepsic digestion in hydrochloric acid [16], which is a common treatment method to achieve ECM printability. The results showed that 97.39% of particles were less than 200 μm in size (Fig 2b and c), which also met the printing requirements.

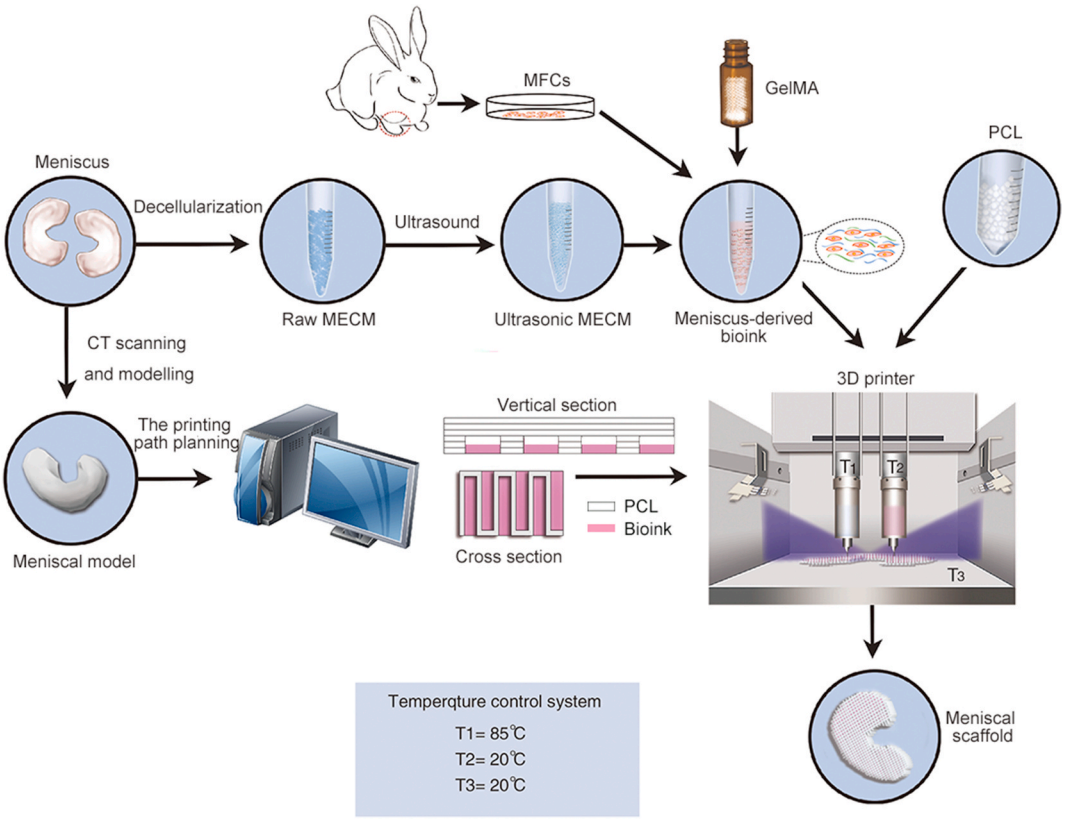

Fig. 1. Process of printing the biomimetic meniscal scaffold. The bioink was prepared by mixing ultrasonicated MECM, GelMA and MFCs at specific concentrations. Meanwhile, the sheep meniscus was scanned by CT, modeled in Mimics, and used to plan the printing path. The prepared bioink and PCL were printed under the designed printing parameters according to the established printing path, and finally, printing of the biomimetic meniscal scaffold was completed.

Moreover, the effects of three treatments on the composition of MECM were compared. Firstly, ultrasonication and digestion by pepsin both obtained a uniform suspension compared with the raw MECM (Fig. 2d). Additionally, the SEM results showed that there was a network of large molecular chains in raw MECM that became smaller after ultrasonication, and these molecular chains became even smaller and blocky after digestion by pepsin (Fig. 2e). The results of type I collagen immunofluorescence showed that the difference between raw MECM and ultrasonicated MECM was not obvious, while the fluorescence intensity of MECM treated with pepsin was significantly decreased (Fig. 2f). The quantitative results by the kit also supported the above analysis. The ratio of collagen in ultrasonicated MECM/raw MECM was 0.946 ± 0.014 mg/mg (mean ± SD), and that in MECM subjected to pepsic digestion compared to raw MECM was 0.658 ± 0.044 mg/mg (mean ± SD) (Fig. 2g), which is similar to previous results [16].

3.2. Cytocompatibilty of meniscus-derived bioink

By mixing the different materials at specific concentrations, we completed preparation of the meniscus-derived bioink. Since this study is the first to ultrasonically treat MECM, this experiment verifies the effect of ultrasonic MECM by comparing GelMA and GelMA/MECM. Cell toxicity and proliferation were analyzed by a Cell Counting Kit 8 (CCK-8) assay. After 5 days of culturing, more MFCs were observed in the GelMA and GelMA/MECM groups than in the control (Fig. 3a), while at the other time points, there is no significant difference, indicating they do not have cell toxicity and apparently enhance proliferation. In addition, chondrogenic genes of MFCs encapsulated in GelMA and GelMA/MECM hydrogels were analyzed. The results showed that the addition of MECM made a positive impact on the expression of COL I and COL II genes , while there is no merit on the chondrogenesis transcription marker like SOX9 (Fig. 3b). The above results were further confirmed in immunofluorescence staining. As shown in the images, COL I (Green) produced by MFCs in GelMA/MECM was significantly more than in GelMA at 3days and 14 days. However, compared with COL I at 3days, an apparent increase was not observed at 14 days, which was probably caused by its exudation from hydrogels. Moreover, with the prolonging of culturing time, cell (DAPI, blue) proliferation was significant in GelMA and GelMA/MECM, although the difference between two groups was not obvious. We also evaluated cell adhesion and migration in hydrogels by F-actin (Red). Initially, all cells were spherical and distributed evenly in hydrogels (Supplementary Fig. 3) . At 3days, a few MFCs displayed a spindle morphology in GelMA, while a greater number of MFCs spread sufficiently in GelMA/MECM at 14days, almost all MFCs in GelMA showed a dendritic morphology, indicating a substantial increase of actin. On the contrast, besides these, the cells in GelMA/MECM were also observed to be elongated and created mesh-like junctions (for additional details referring to Supplementary Fig. 4), which showed the addition of MECM was meaningful for the adhesion and migration of MFCs and the repair of cartilage maybe benefit from it [24].

3.3. Rheological characterization and printability of meniscus-derived bioink

Comprehensively understanding the rheological characteristics of the bioink is helpful for estimating the shear force to that cells are subjected to during the 3D printing process. As shown in Fig. 4, with increasing oscillation frequency, the instability of GelMA became more obvious compared with that of GelMA/MECM (Fig. 4a), while there was little disparity on the shear thinning for the two bioinks (Fig. 4b). The bioink's viscosity both gradually declined with the rise of shear rate. In

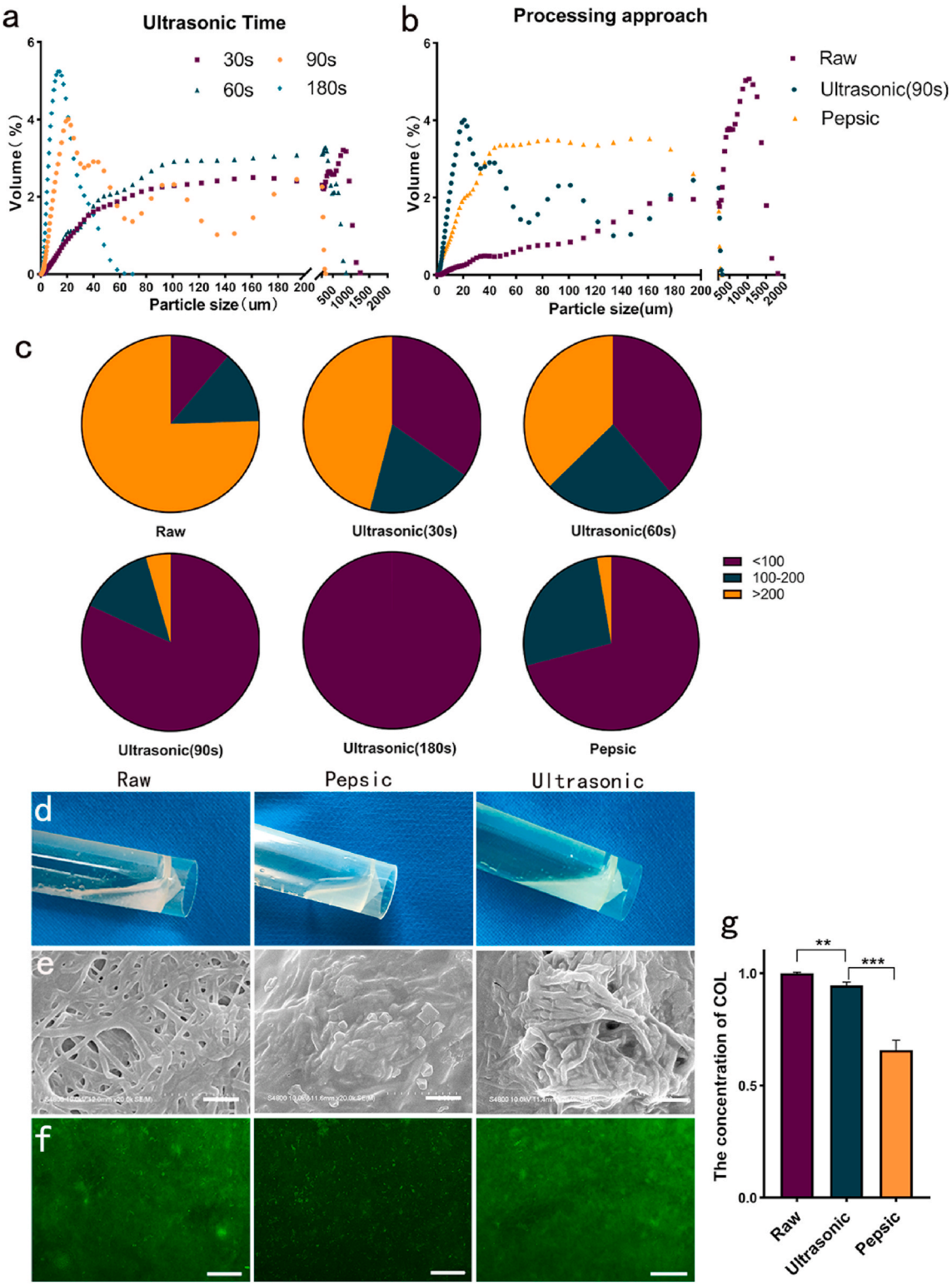

Fig. 2. Characterization of printable MECM. (a) Effect of ultrasonication time on the particle size of MECM. (b) Effect of treatment method on the particle size of MECM. (c) Quantitative distribution of the particle size. (d) Gross observation. (e) SEM images (scale bar: 1 μm). (f) Type I collagen immunofluorescence images (scale bar: 500 mm). (g) Quantitative analysis of the collagen concentration (**P < 0.01, ***P < 0.001).

addition, the experiment analyzed the effect of temperature on the kinetics of gelation. The two bioinks showed high sensitivity to temperature; that is, as the temperature decreased, the viscoelasticity decreased (Fig. 4c). When the temperature reached the gelation temperature, the elastic modulus increased rapidly, indicating that the bioink began to transform from a fluid to a colloid, which is a prerequisite for printing a hydrogel with good shape fidelity. More visualized displays were in gross observation. With the change of temperature, GelMA/MECM turned to be colloid (Fig. 4e) from fluid (Fig. 4f). GelMA showed the same characteristic (Fig 4i and j). The gelation temperature of GelMA/MECM was 24 °C, and that of GelMA was 19 °C. The addition of MECM raised the gelation point of GelMA. The temperature sensitivity of the

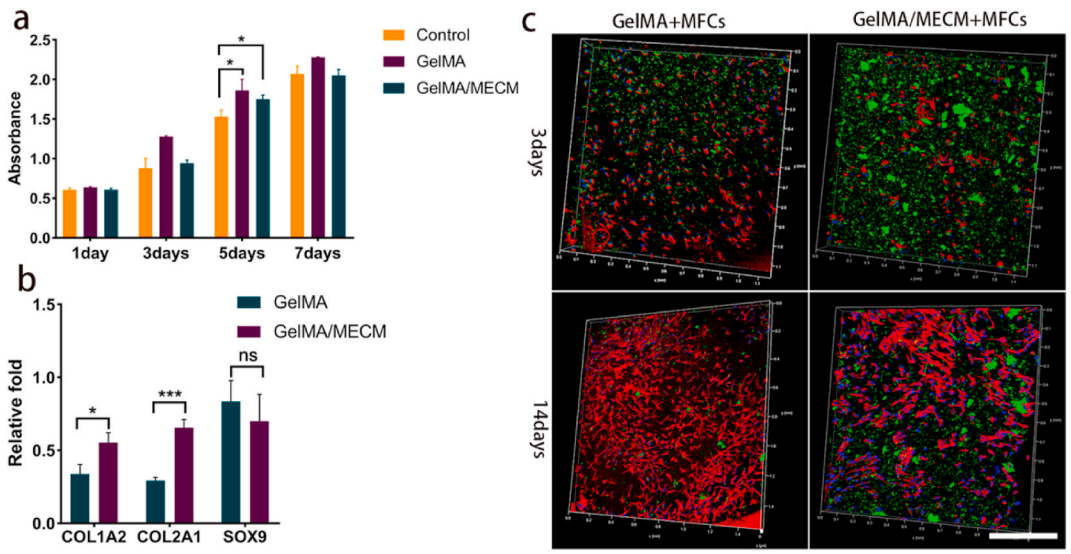

Fig. 3. Cytocompatibility of the meniscus-derived bioink. (a) CCK-8 assays results of MFCs cocultured with different hydrogels for 1–7 days. (b) Comparative gene expression analysis for chondrogenic SOX9, COL1A2 and COL2A1 in GelMA and GelMA/MECM at 14days. (c) Immunofluorescence images showing the chondrogenic phenotype of MFCs in GelMA and GelMA/MECM constructs by COL type I staining (Green), cell nuclei (DAPI, blue) and F-actin (Rhodamine-phalloidin, red) (scale bar: 500 μm). (For interpretation of the references to color in this figure legend, the reader is referred to the Web version of this article.)

two bioinks showed a certain time delay (Fig. 4d). When the temperature dropped rapidly from 37 °C to the gelation temperature, the viscoelasticity of GelMA/MECM started to increase rapidly and reached a preliminary stability at 3 min. After that, the storage modulus increased slowly, while the loss modulus showed a steady trend, and both were essentially stable at 30 min. Compared with GelMA/MECM, GelMA showed a more obvious delay in viscoelasticity with the variation in temperature, and its viscoelasticity increased relatively slowly. The loss modulus was almost stable at 10 min, whereas the storage modulus was not stable until 30 min. In addition, we compared the viscoelasticity of GelMA/MECM hydrogels at different temperatures and found that lower temperatures led to significant increases in the storage modulus of the bioink from 408.0 Pa to 1943.3 Pa but little change in the loss modulus from 17.5 Pa to 13.4 Pa. These findings indicated that fluctuations of the printing temperature may have a certain effect on the shear force experienced by cells. In general, the addition of MECM improves the temperature-sensitive delay exhibited by GelMA, thereby increasing the stability of the printing process.

Bioinks with good printability are useful for creating high-precision and stable constructs. General observations did not identify obvious differences between the fidelity of the bioinks (Fig. 4g, k). Microscopic observations (Fig. 4h, l) and quantitative analysis (Fig. 4m) showed that the spreading ratio of GelMA/MECM was 2.49 ± 0.12 and that of GelMA was 2.62 ± 0.52. There was little difference between the two groups, but the strand of GelMA + MECM was more uniform and stable.

3.4. Development of the biomimetic meniscal scaffold system

The keys to printing the biomimetic meniscal scaffolds were the coordination of the two printing materials and the feasibility of the complex meniscal model. Consequently, the development of the system was divided into two parts: printing of the primary model to explore the printing conditions of each material and coordinate them, and printing of the biomimetic meniscal model to solve the unknown problems in the complicated process. Firstly, we explored the conditions for printing the primary model, including hydrogel (GelMA/MECM) (Fig. 5a, left) and PCL (Fig. 5b, middle) with a single nozzle, respectively, and a simple square model (PCL + hydrogel) with dual-nozzle (Fig. 5a, right). As shown in the figures, every construct was printed with high precision (Fig 5b–d). The meniscal model was then studied. Printing of the biomimetic meniscal scaffold was a complicated process (Fig. 5e) that required the adequate knowledge of all details of the printing process. However, this complexity and the comprehensive study of the primary model together contributed to the high success rates and precision of the biomimetic construct according to the model designed (Fig. 5f). Finally, we achieved the printing of the biomimetic meniscal scaffold (Fig. 5e, Supplementary video 1). The actual diameter of the hydrogel strands was 992.4 ± 28.6 μm and that of the PCL strands was 515.2 ± 23.65 μm (Fig. 5g), which primarily verified the feasibility of the biomimetic meniscal printing system.

3.5. Cell viability

Shear force is the main factor that causes cell damage during printing. In the dual-nozzle printing model, the high-temperature PCL, long printing time and relatively insufficient exchange of substance may also affect cell viability. Thus, the cell viability in structures printed via a single nozzle and dual nozzles was tested. We observed that the cell viability was 90.92 ± 2.10% after single-nozzle printing and 90.03 ± 2.69% after dual-nozzle printing (Fig 6a, d), indicating the good performance of the parameters of the dual-nozzle model. In the meanwhile, the panoramic scanning (4×4) displayed the bulk of the constructs printed by single nozzle (Fig. 6b) and dual nozzles (Fig. 6c), and similar cell viability was observed. In addition, we cultured the two constructs for 14 days. The cell viability of the constructs produced by single nozzle and dual-nozzle printing was 96.87 ± 0.22% and 99.14 ± 0.14%, respectively. Compared with that at 1 day, there was a slight increase in viability (Fig 6a, d), demonstrating that the scaffold had good cytocompatibility and provided the effective space for the exchange of nutrients and oxygen.

3.6. Biomechanical analyses

In dual-nozzle printing, unreasonable parameters and the model design lead to unstable and unrepeatable constructs. Therefore, in addition to investigating the biomimetic mechanical properties for human menisci, we also sought to demonstrate the stability and repeatability of the scaffold by mechanical tests. In the compression test, samples in the PCL + hydrogel group and the PCL group exceeded the elastic deformation range at 9.36% and 9.26%, respectively, and these

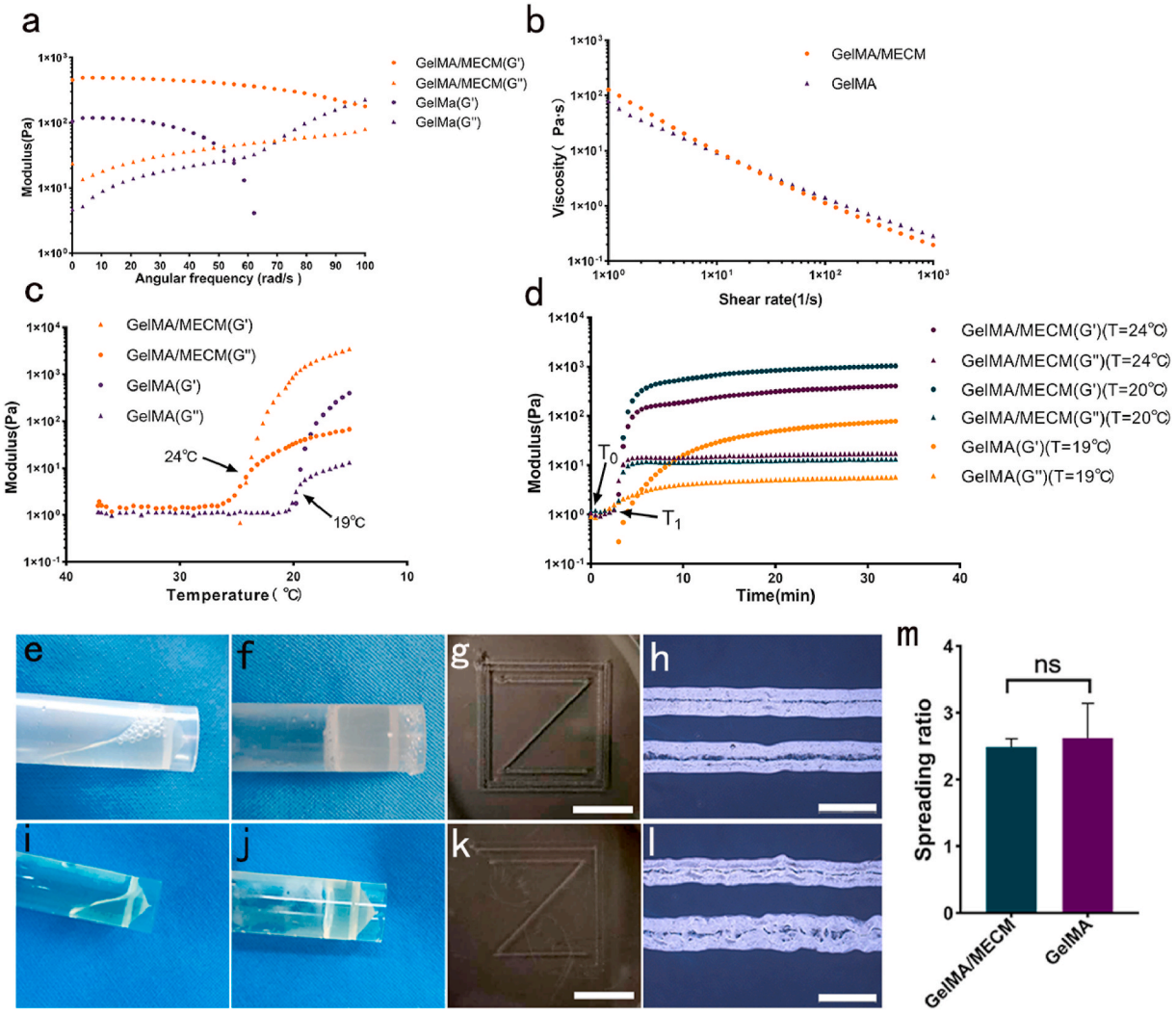

Fig. 4. Rheological characteristics and printability of the bioinks. (a–d) Rheological characteristics of the bioink: (a) Loss modulus (G″) and storage modulus (G′) at different angular frequencies. (b) Variation in viscosity with varying shear rate at the gelation temperature. (c) Gelation kinetics from 15 °C to 37 °C. (d) Variations in loss modulus (G″) and storage modulus (G′) from 37 °C (T_0) to a fixed temperature (T_1, referring to legends). The above experiments were repeated in triplicate. GelMA/MECM's transition of state from sol at 37 °C (e) to gel at 20 °C (f). (g) Printability of GelMA/MECM (scale bar: 1 cm). (h) GelMA/MECM hydrogel under a light microscope (scale bar: 1 mm). GelMA's transition of state from sol at 37 °C (i) to gel at 15 °C (j). (k) Printability of GelMA (scale bar: 1 cm). (l) GelMA hydrogel under a light microscope (scale bar: 1 mm). (m) Spreading ratio of the bioinks (ns: $P > 0.05$).

values were similar to the physiological compression strain in humans (10%). Additionally, the samples showed good rebound (Fig. 7a). The compressive modulus in the PCL + hydrogel group was 12.63 ± 2.10 MPa, which was lower than that in the PCL group, at 22.48 ± 1.04 MPa (Fig. 7b). These results were probably caused by the interaction of the two materials. Concerning the tensile test, the PCL + hydrogel samples remained within the elastic strain scope, while the PCL samples exceeded the range at 2.67% (Fig. 7c), which was considerably different from the estimated physiological strain (5%). The tensile modulus in the PCL + hydrogel group was 24.86 ± 0.43 MPa, which was less than that in the PCL group, at 30.59 ± 1.93 MPa (Fig. 7d). Moreover, the small within-group difference verified the stability of dual-nozzle model.

3.7. Subcutaneous degradation

The biodegradation of hydrogels in the scaffolds was analyzed by subcutaneous implantation (Fig. 8c). During the experimental process, one mouse in the PCL group died after 3 days for unknown reasons. We observed that the fluorescence intensity of the PCL + hydrogel did not change significantly in PBS (Fig. 8a, Supplementary Fig. 5), indicating that fluorescence quenching will not occur in the dark over time and that the fluorescence will not decrease without biodegradation. These results are similar to that of other researches [25], whereas there were different degrees of biodegradation in the hydrogel group (Fig 8a and b). On imaging, we selected the region of interest (ROI) to quantitatively calculate the fluorescence intensity. At 14days, the remaining fluorescence intensity in the hydrogel group and the PCL + hydrogel group were 24.42 ± 0.79% and 67.95 ± 14.74%, respectively. The biodegradation rate in the PCL + hydrogel group was significantly slower than that in the hydrogel group ($P < 0.05$). It might be reasonable to assume that the PCL framework had a protective effect on the internal hydrogel and slowed biodegradation. At 21 days, the remaining fluorescence intensity was 7.51 ± 13.00% in the hydrogel group, and at 28 days, it was 19.33 ± 17.43% in the PCL + hydrogel group, showing that the full degradation time was slightly prolonged. Dissection was carried out after finishing the test (Fig. 8d).Residual hydrogel or obvious signs of inflammation, including redness, swelling and bleeding, were not observed [26].

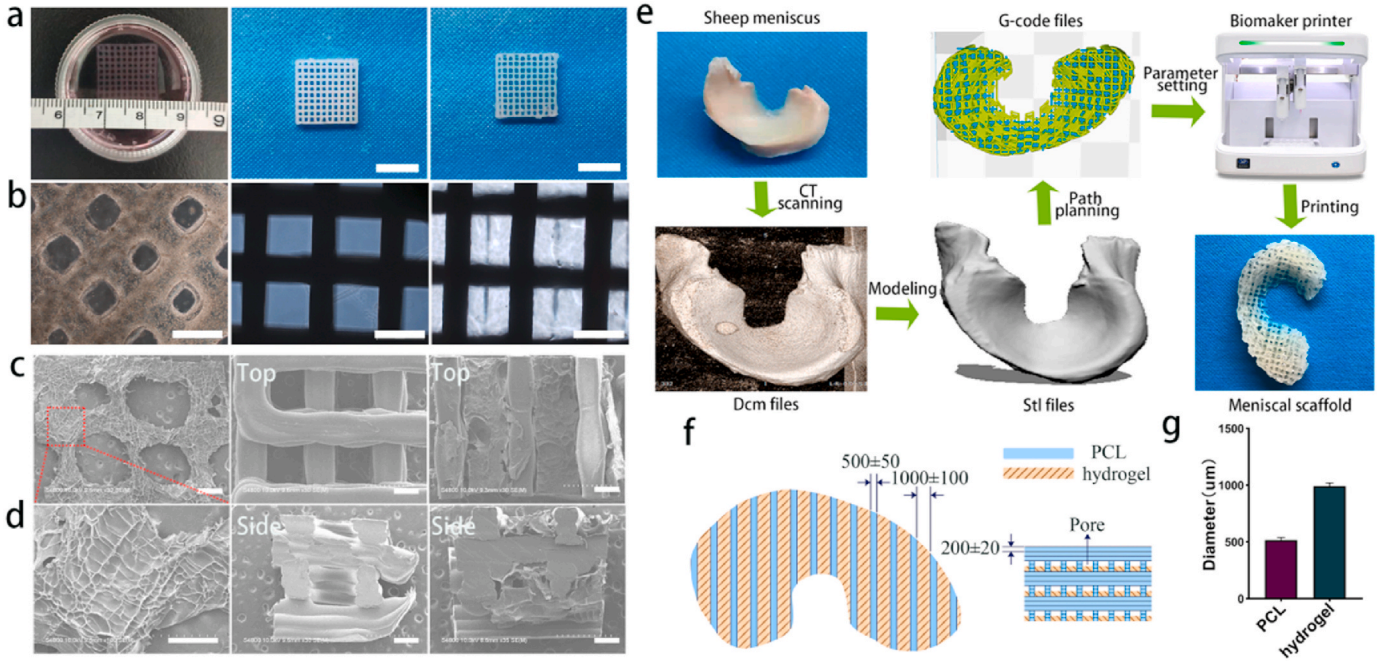

Fig. 5. Development of the biomimetic meniscal scaffold system. The primary model(a-d): the gross observations (a) (scale bar:1 cm), the microscopic images (b) (scale bar: 1 cm) and SEM images (c, d) (scale bar: 500 μm) of the hydrogel scaffold ("GelMA/MECM" hydrogel, abbreviated as "hydrogel" in subsequent experiments), PCL scaffold and simple square scaffold from left to right. (e) Process of printing the biomimetic meniscal scaffold. (f) Specific details of the meniscal model. (g) Actual diameter of the strands of the meniscal scaffold.

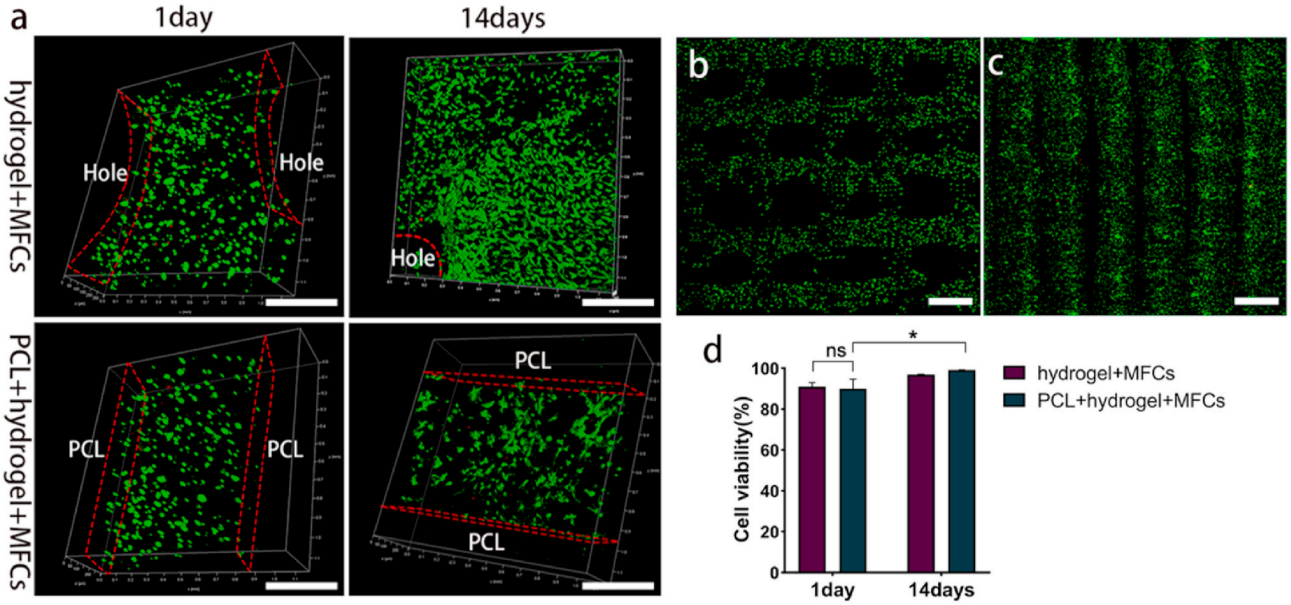

Fig. 6. Cell viability after printing with a single nozzle (hydrogel+MFCs) and dual nozzles (PCL+hydrogel+MFCs). (a) Confocal images of two constructs after live-dead staining at two time points (scale bar: 500 μm). The panoramic scanning (4×4) of the constructs printed by a single nozzle (b, black part was hole) and dualnozzles (c, black part was PCL) at 1 day (scale bar: 1 mm). (d) Quantitative results for cell viability (*P < 0.05, ns: P > 0.05).

3.8. Degradation in situ

The biodegradation of PCL in the scaffolds was analyzed by implantation in situ. The general effectiveness was divided into three terms as depicted in Table 2. Due to unexplained meniscal tears in the PCL group at 6 months, two implants were lost. With regard to the integrity of implants, at 3 months, limited differences were observed between the two groups and slight damage had occurred. At 6 months, there was no visible scaffold, but the sutures of some implants were observed in the reborn tissue (for additional details, referring to dissecting specimens in Supplementary Fig. 6). In terms of the regenerative tissue, at 3 months, implants of the two groups were mostly able to integrate into the new tissue. At 6 months, it was clearly seen that the reborn tissue filled the defect in the PCL + hydrogel group, while the PCL group just had the last one implant that repaired the defect (Fig. 9a).

Additionally, histological and mechanical analyses of the PCL + hydrogel constructs were performed. Histological staining indicated that collagen type I and glycosaminoglycans (GAGs) initially formed at 3

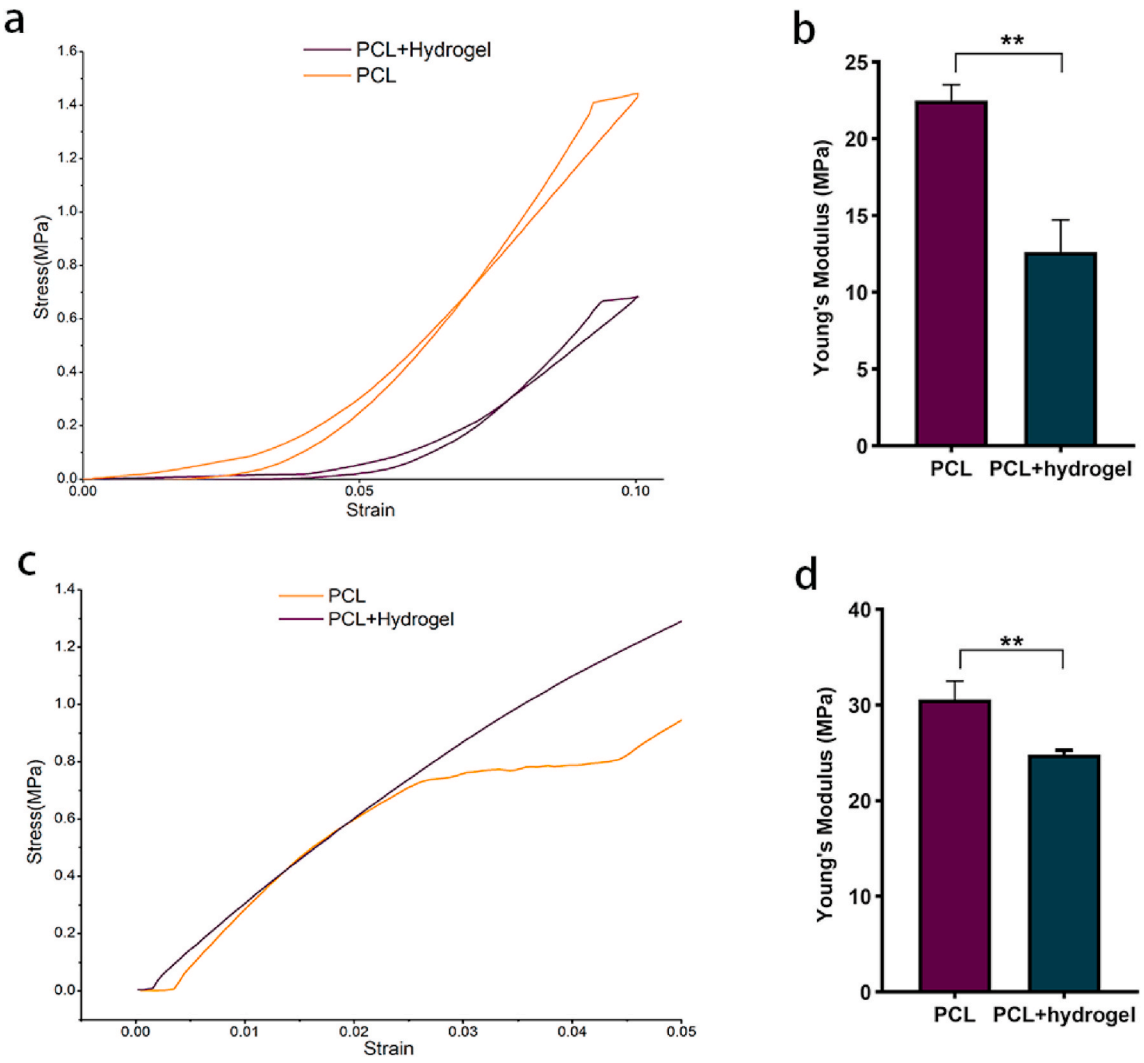

Fig. 7. Mechanical properties of the scaffolds printed by single nozzle and dual-nozzle. (a) Compressive stress-strain curve. (b) Compressive Young's modulus (**P < 0.01). (c) Tensile stress-strain curve. (d) Tensile Young's modulus (**P < 0.01).

months, and well-ordered collagen type I was discovered at 6 months (Fig. 9e). By contrast, the compressive modulus was still an order of magnitude lower than that of the native meniscus (Supplementary Fig. 7), which suggested that the neotissue had poor function and still required further reconstruction. The biodegradation of the PCL framework was reflected by the molecular weight measurements and the nanoindentation experiment in the PCL + hydrogel group. The results showed that the molecular weight of PCL did not vary substantially at 3 months but was significantly reduced at 6 months (Fig. 9b). The elastic modulus and hardness also presented the similar trend (Fig. 9c and d).

3.9. Tissue formation in vivo

The formation of collagen was assessed by PR staining and collagen type I immunohistochemistry, and the production of GAGs was judged by TB staining. In PR staining, strong, birefringent, red and yellow fibers represent collagen I, weak, birefringent, multicolor, loosely networked fibers represent collagen II, and weak, birefringent, green fibers represent collagen III. Generally, there is no obvious degradation of the PCL frame in each group, and the gap among newborn tissue represented its location. Because it was difficult for the implants to perform intact frozen sections, the boundary of the PCL frame and newborn tissue was not clear. In Fig. 10, it was clearly shown that there was little effect on enhancing the formation of cartilage tissue in the PCL group at two time points. By contrast, some collagen and GAGs could be observed in the other groups at 4 weeks. Furthermore, neotissue gradually displayed an ordered arrangement in the PCL + hydrogel group at 8 weeks, especially based on the collagen type I immunohistochemistry, while more newborn tissue was observed in the PCL + hydrogel +MFCs group, indicating that the cells played a role for tissue regeneration.

4. Discussion

With the development of multi-nozzle printing technology [27–29], many researchers have attempted to apply it to different medical fields [30,31].In this study, a customized printing system and meniscus-derived bioink were designed according to the characteristics of the meniscus to pursue improved performance and provide a feasible solution for the treatment of meniscal injury by tissue engineering.

Well-designed biomimetic constructs can provide a suitable microenvironment for the regeneration of meniscal tissue. Thus, in this study, we attempted to develop meniscus-derived bioinks with both printability and satisfying cytocompatibility. Bioinks currently applied for 3D bioprinting are mainly composed of natural polymers, including sodium alginate, gelatin, collagen, chitosan, fibrin, hyaluronic acid, and ECM [32–38]. Among them, ECM, which retains most of the native components and lacks cellular immunogenicity, is an ideal biological material that can promote cellular proliferation and differentiation [39,40].

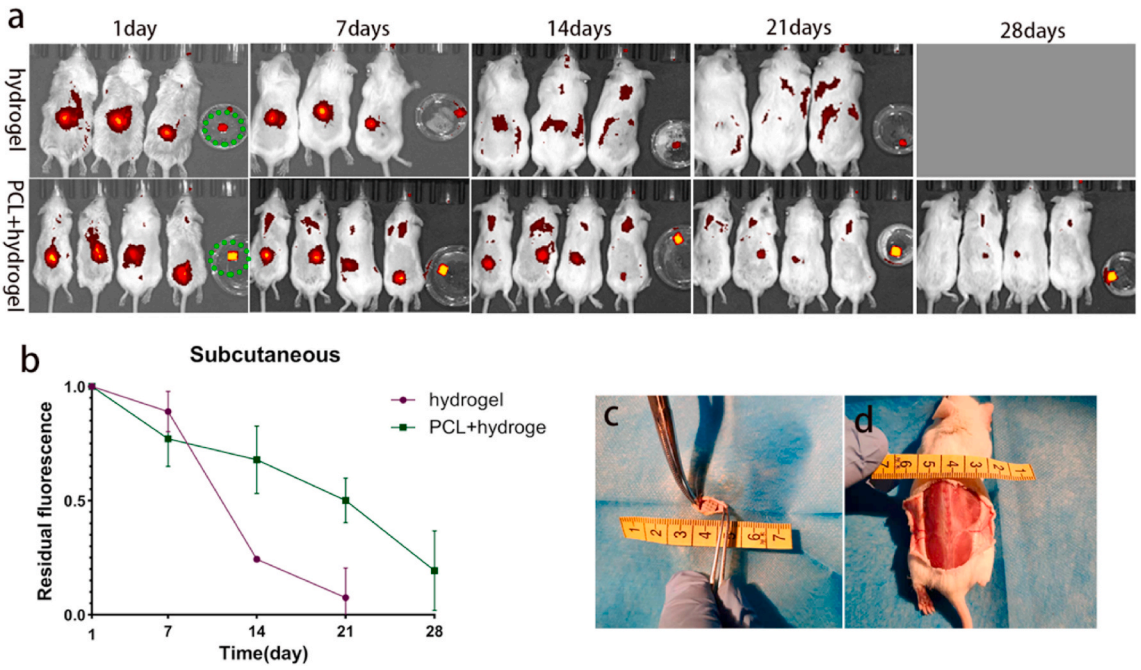

Fig. 8. Quantitative fluorescence analysis of subcutaneous hydrogel degradation. (a) Variation in the fluorescence intensity of all specimens. The specimens in green circle cultured in PBS as control group. (b) Quantitative fluorescence analysis of three subcutaneous specimens from each group. (c) The process of surgical operation. (d) Dissection of the samples' position after the fluorescence disappearance. (For interpretation of the references to color in this figure legend, the reader is referred to the Web version of this article.)

Table 2
The status of implants and regenerative tissue. Each parameter was scored from 1 to 3.

Features	PCL+hydrogel								PCL							
	3 months				6 months				3 months				6 months			
	S1	S2	S3	Mean	S4	S5	S6	Mean	S7	S8	S9	Mean	S10	S11	S14	Mean
Implant position	3	3	3	3.0	3	3	3	3	3	3	3	3	1	1	3	1.7
Integration	3	2	2	2.3	1	1	1	1	3	2	1	2	1	1	1	1
Tissue	2	2	2	2	3	3	3	3	2	2	1	1.7	3	1	1	1.7

However, due to the complex components of ECM, it is insoluble in water and organic solvents; hence, ECM is difficult to extrude from a printing nozzle. To achieve the printability of ECM, Donald O. Freytes et al. [16] firstly used pepsin and hydrochloric acid to dissolve it and then adjusted the temperature to form a hydrogel for more than 30min, but its relatively long gelation time is not suitable this model. In addition, Lin [41] found that, compared with collagen I, pepsin-digested ECM did not show the obvious advantages of improving the behaviours of cells. Therefore, for the first time, this research developed a comparatively simple method based on ultrasound [42] was used to treat MECM to yield a small particle size with a uniform distribution within the printable range. However, this study only uses collagen I to reflect the effect on the overall composition of MECM, thus further research is needed to determine changes in more active constituents. Since MECM alone shows a poor gelation performance and unsatisfactory shape fidelity. GelMA, a derivative of gelatin, was introduced in this experiment. Reversible temperature-sensitive gelation coupled with simple and fast photocrosslinking resulted in a broad range of applications for GelMA. Moreover, its great biocompatibility makes it an excellent option [43,44]. Therefore, in this study, the meniscus-derived bioink that presented both printability and cytocompatibility was formulated by mixing MECM with GelMA at specific concentrations.

Many factors influence the behaviours of cells in the three-dimensional culture of hydrogels, including the composition, concentration, viscoelasticity [45], mechanical properties [46], etc. These properties often influence each other and it is hard to control a single variable. In the study, the ECM digested with pepsin and the meniscus-derived bioink (GelMA/MECM) were quite different in terms of viscoelasticity and mechanics, so we did not compare the two bioinks. By comparing GelMA and GelMA/MECM, the function of ultrasonic MECM was initially explored. However, due to the complex components of MECM, it is difficult to prove which components played a role. This study only preliminarily proved that MECM played a certain role in promoting collagen secretion and cell extension, and the functions of specific components and whether other positive effects occur require further research.

Analyzing the characteristics of bioink is essential for optimizing the printing parameters. Some researchers have investigated the rheological performance of GelMA [47] and revealed certain stability and shear-thinning properties. The results of subsequent research fully characterizing the rheological features of GelMA/MECM showed that the bioinks have analogous features. In addition, this study reveals that GelMA/MECM bioink is sensitive to temperature and has an obvious delay, with more than 30 min required to reach stability. Because of the mutual thermal interference between parts during printing, there may be some fluctuations in the viscoelasticity of GelMA/MECM that can influence the smoothness of printing and the viability of cells. Accordingly, in this study, a motor drive was selected over a pneumatic drive; thus, even if GelMA/MECM exhibits certain changes in viscoelasticity due to temperature fluctuations, the smoothness of the printing process

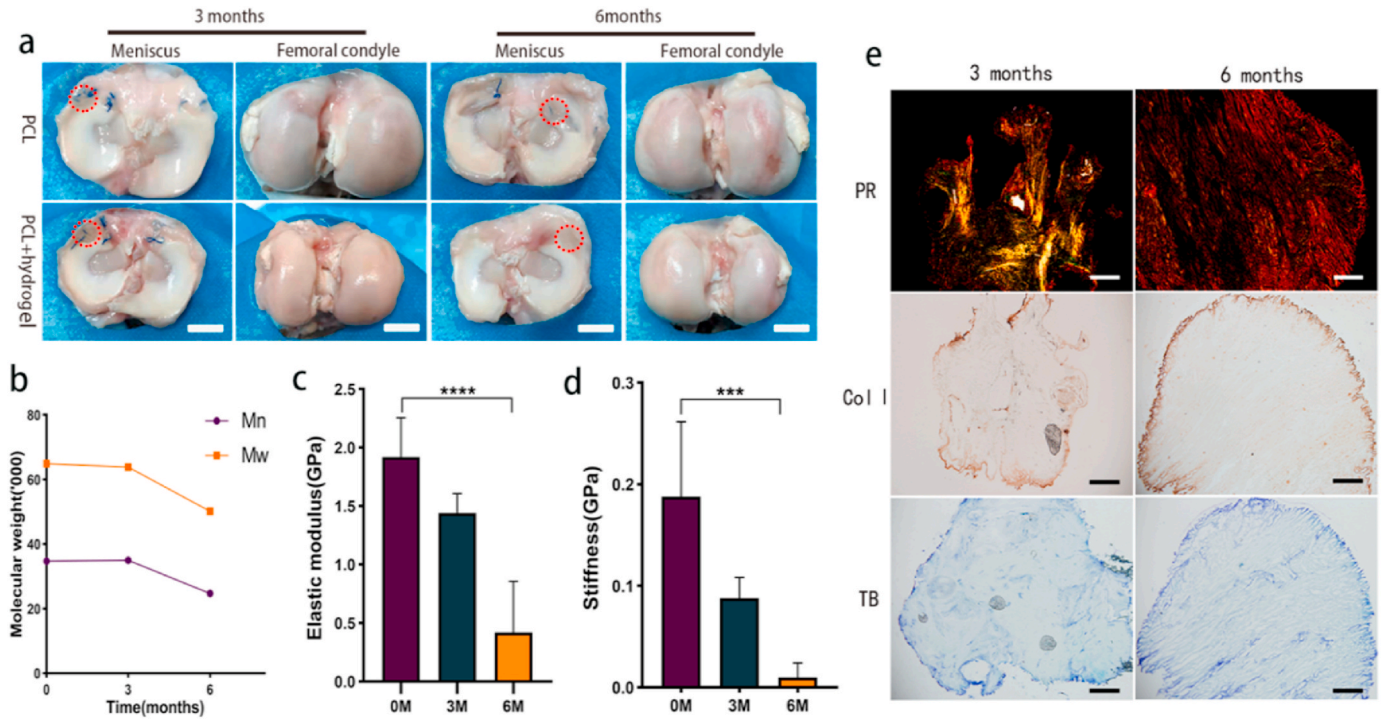

Fig. 9. Analysis of the biodegradation of scaffolds in situ. (a) Gross view of the implant and femoral condyles (scale bar: 1 cm) , with the implants location shown in red circles. (b) Variation in the molecular weight of PCL. (c) Variation in the elastic modulus of PCL (****P < 0.0001). (d) Variation in the hardness of PCL (***P < 0.001). (e) Histological evaluation by collagen type I immunohistochemistry and picrosirius red (PR) and toluidine blue (TB) staining (scale bar: 500 μm). (For interpretation of the references to color in this figure legend, the reader is referred to the Web version of this article.)

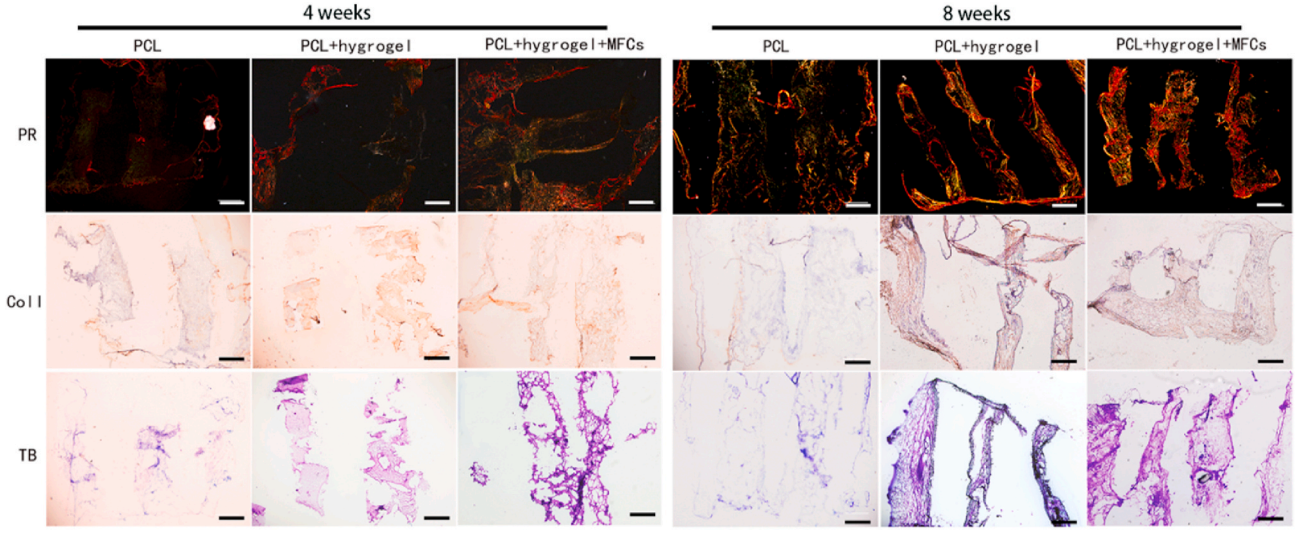

Fig. 10. Preliminary evaluation of the regenerative effect of scaffolds in a nude mouse model (scale bar: 500 μm).

will not be apparently disturbed. In addition, the printing temperature was set to 20 °C to prevent the material from transitioning from gel to sol under the high temperature of the PCL nozzle.

Multi-nozzle printing technology significantly expands the range of materials that can be selected, which is conducive to the construction of complex 3D models. However, the coordination of different nozzles and different materials still involves many details. Therefore, it is necessary to explore the printing conditions for each material. In terms of the printing of cell-laden hydrogels [48,49], there are a few differences based on the type of bioinks and cells. In this research, to ensure high fidelity and high cell viability (greater than 90%), various parameters, including the GelMA/MECM concentration ratio, the inner diameter of the nozzles, the printing temperature, and the printing speed, were repeatedly adjusted. The printing of PCL is relatively simple, and the only key point is adjusting the printing temperature and speed. The challenge in this study was coordinating the two nozzles and materials well to simultaneously guarantee the structural stability, cell viability and desired mechanical properties. When we explored the conditions for dual-nozzle printing of the preliminary square model, the first problem we encountered was the instability of the printed construct, which was prone to delamination under external forces. Thus, the printing model was modified to print of PCL strands three times with the aim of ensuring that the height of the PCL strands exceeded that of the hydrogel strands in each layer, thus allowing the PCL strands in the different layers to

firmly bond. This approach had a few merits, including ensuring the stability and fluency of the printing process, preventing delamination of the construct and damage to cells, and generating some pores for cells to supply oxygen and nutrients. Because the stability of the entire structure purely depends on the bonding of intersecting PCL strands, the diameter of the PCL strands must not be excessively thin because this parameter directly influences the bonding area at the intersection. Moreover, the hydrogel strands cannot be excessively narrow either; otherwise, the hydrogel, on account of the hydrophobic character of PCL, cannot firmly combine with the PCL strands and may even float out of the framework after immersion in medium. More importantly, thin strands would easily dry out during the long printing process. In addition, the printing temperature is key to maintaining printing stability. Since the viscosity of PCL decreases with increasing temperature, higher printing temperatures may allow the PCL strands to deposit on the hydrogel strands more easily under gravity, which would affect both cell viability and the shape of the construct. However, lower printing temperatures are not conducive to the bonding of two PCL layers. After repeated trials, 85 °C was eventually determined to be the optimal PCL printing temperature, and the hydrogel printing temperature of 20 °C was determined based on the gelation kinetics. The printing platform temperature of 20 °C is also a decidedly prominent condition, contributing to preventing the GelMA/MECM gel from transforming into a solution due to the relatively higher room temperature before crosslinking. Otherwise, pore formation may be disrupted. In fact, a full understanding of the materials and printing principles is required to resolve key issues in the whole process, and such an understanding will allow for the smooth creation of many customized models in different areas.

Cell viability and mechanical properties were the preliminary criteria used to verify the success of the model in this study. Many factors, including the bioink components [50,51] and the printing model and parameters [52], influence cell viability in printing process. As there have been few related studies on printing MFCs and GelMA/MECM hydrogels, we refer to some studies of dual-nozzle printing with live cells. Joydip Kundul [53] printed PCL and chondrocytes encapsulated in a sodium alginate hydrogel and found that the cell viability reached 85%. S. Romanazzo [54] wrapped fat pad-derived stem cells in an alginate-ECM hydrogel and then printed them with PCL, and the cell viability was maintained at 80%–90%. In this study, cell viability tests were performed using both single nozzle and dual-nozzle printing followed by culturing for 1 day and 14 days in vitro. The cell viability exceeded 90%. Moreover, the hydrogel was cultured for up to 6 weeks (Supplementary Fig. 8), and the cell viability remained above 90%. These data prove the feasibility of the printing model and good cytocompatibility of the materials used in this research. Except for these, cell proliferation in the single-nozzle model was significantly better that in dual-nozzle model, which may be caused by relative reduced superficial area for the exchange of substance, despite we have designed the pores in the dual-nozzle model. In fact, pores are essential for the similar model, which even decrease the cell viability as previously reported [55].Therefore, how to better solve the issue still require a more ingenious design.

Currently, multi-nozzle printing model has been applied in many medical fields, but some researchers has not performed mechanical tests [29,31,53], while others have only carried out partial tests [13,56]. Hence, we have tested some valuable mechanical properties related to the meniscus and summarized them. Generally, there are three vital problems in the dual-nozzle printing model. First, the stability of the construct, i.e. the delamination as mentioned above, principally impacts on the mechanical test and the suture of experiments in vivo. Obviously, the most simple and effective way of resolving this issue is declining the quantity of the bioink, which probably influence the repair effect in animal tests, thus we designed a new model in this study. Second, the uniformity of the scaffolds printed by different batches is hard to guarantee, particularly for the temperature-sensitive materials. The most important cause is the deficiencies of printer, such as unstable temperature control, and a lack of knowledge on the materials, such as an inadequate melt of PCL and fluctuant modulus of the bioink. Thirdly, there is a gap of mechanical properties is observed between the scaffold and native tissue, which is definitely restrained by the materials and models. As a whole, this study has resolved the issue of stability and uniformity, and in terms of mechanical properties, we have tried to increase the PCL strand spacing and decreased the PCL strand diameter to achieve better mechanical biomimetics. Eventually, the PCL strand diameter was set to 500 μm and spacing was set to 1000 μm. The compression modulus of the construct was 12.63 MPa, which is higher than that of the human meniscus (0.3–2 MPa) [57,58]. In addition, limited by the integral model, the tensile modulus was 24.86 MPa, which is close to that of the meniscus in the radial direction (4–20 MPa). However, compared with the circumferential tensile modulus (78–120 MPa) [59], there is still a large disparity. These findings are similar to those of other studies [8,9].

In regenerative medicine, the ideal goal is to perfectly match the degradation rate to the regeneration rate [60]. If the scaffold degrades too quickly, then the support for tissue growth will be greatly decreased, while excessively slow biodegradation will hinder regeneration and can even prompt fibrosis [61,62]. It is certainly crucial for researchers to evaluate biodegradation and optimize regeneration. Although there have been numerous related studies on PCL degradation, the main assessments were performed in vitro, such as in PBS [63,64], an acid or base [65], or an enzyme [66,67]. Some scientists have also tried to study biodegradation in the rabbit skull [63]; however, the evaluation of orthotopic implants in large animals is not common. In general, the present research confirms that the biodegradation rate of PCL is associated with the initial molecular weight. The early stage mainly involves a decrease in molecular weight, while a decrease in quality gradually occurs in the later stage. The complete biodegradation of PCL takes a long time (several years). The biodegradation of hydrogels is chiefly determined through decreases in quality or volume, and such assessments will require a large number of animals and involve many uncontrollable factors and sources of error. With the development of fluorescence imaging technology [68–70], hydrogels can be continuously monitored in vivo in a noninvasive manner, thus providing an effective and reliable method for assessing the biodegradation of hydrogels. This study took these factors into consideration and designed a customized biodegradation research scheme combined with available technology. Firstly, we cultured printed cell-laden hydrogel scaffolds for up to eight weeks to verify the essential stability (Supplementary Fig. 9). Then, we implanted the scaffold in situ to evaluate the biodegradation of the PCL and implanted the Cy7-labeled scaffold subcutaneously in mice to monitor the degradation of the hydrogel by in vivo imaging. Our results showed that biodegradation of the hydrogel in the scaffold required approximately one month, which is similar to the findings of a previous report [71]. The molecular weight and results of the nanoindentation test were used to evaluate the degradation of the PCL framework in situ. The results regarding the biodegradation of the PCL structure were analogous to those of other studies. The molecular weight of the scaffold was not markedly different at 3 months but was lower to a certain extent at 6 months. However, some of the scaffolds started to show damage at 3 months, and only the remains of these scaffolds were visible at 6 months. It may be that the initial microenvironment has little effect on the integrity of the scaffold, and the strength of the scaffold gradually weakened with the prolonged exposure to forces and the decrease in molecular weight, thus leading to the above results. This result reveals that the mechanical environment of the meniscus may play a decisive role.

The nude mouse model is a primary method used to observe the formation of tissue-engineered cartilage in vivo [72]. The reduced immune system of athymic nude mice allows the implantation of xenogeneic cells. Thus, in this study, scaffolds seeded with cells were implanted subcutaneously into nude mice to analyze the resulting formation of fibrocartilage. Preparing regular cryosections of scaffolds printed using

two nozzles is an arduous process that increased the difficulty of observing portion of the PCL frame that had not actually been degraded in the stained sections. As demonstrated by the results, the GelMA/-MECM hydrogel and MFCs assisted in the formation of meniscal structures, which indicates the biofunctionality of the construct. However, owing to the obvious difference between the subcutaneous microenvironment in nude mice and the native microenvironment of the human meniscus, the scaffold still requires validation in large animal studies.

5. Conclusions

In general, by virtue of a customized dual-nozzle + multitemperature printing system and meniscus-derived bioink, this study fully integrates the advantages of PCL and GelMA/MECM/MFCs to initially achieve a biomimetic scaffold similar to the native meniscus in terms of morphology, mechanics, components, and microenvironment. This approach obviously improves both the level and efficiency of biomimetic meniscal scaffolds in tissue engineering. Furthermore, a variety of experiments were carried out to assure the feasibility and functionality of the scaffold for various applications. However, the scaffold is still different from the native meniscus in some aspects. PCL has substantial hardness and insufficient flexibility. MECM loses its original physical properties after decellularization, and the componential biomimetics is only achieved by the layer-by-layer stacking of materials, which is distinct from the ring-shaped arrangement of highly crosslinked meniscal collagen fibers. Therefore, improvements in materials science and printing technology may be key to advancing in tissue engineering. Currently, the combination of different techniques may be effective for achieving higher-level biomimetics of the meniscus.

Funding

This study was supported by the National Key R&D Program of China (2017YFC1103404) and the National Natural Science Foundation of China (81872070).

CRediT authorship contribution statement

Zhou Jian: Data curation, Investigation, Writing - original draft. **Tian Zhuang:** Data curation, Writing - original draft. **Tian Qinyu:** Resources, Software, Writing - review & editing. **Peng Liqing:** Resources. **Li Kun:** Resources. **Luo Xujiang:** Resources. **Wang Diaodiao:** Resources, Methodology. **Jiang Shuangpeng:** Resources. **Sui Xiang:** Methodology. **Huang Jingxiang:** Methodology. **Liu Shuyun:** Formal analysis. **Hao Libo:** Formal analysis. **Tang Peifu:** Supervision. **Yao Qi:** Supervision, Writing - review & editing. **Guo Quanyi:** Conceptualization, Funding acquisition, Supervision, Writing - review & editing.

Declaration of competing interest

The authors declare that they have no known competing financial interests or personal relationships that could have appeared to influence the work reported in this paper.

Appendix A. Supplementary data

Supplementary data related to this article can be found at https://doi.org/10.1016/j.bioactmat.2020.11.027.

References

[1] N.J. Gunja, D.J. Huey, R.A. James, K.A. Athanasiou, Effects of agarose mould compliance and surface roughness on self-assembled meniscus-shaped constructs, J Tissue Eng Regen Med 3 (7) (2009) 521–530, https://doi.org/10.1002/term.191.
[2] W.M. Weiss, D. Johnson, Update on meniscus debridement and resection, J. Knee Surg. 27 (6) (2014) 413–422, https://doi.org/10.1055/s-0034-1388653.
[3] B.R. Waterman, N. Rensing, K.L. Cameron, B.D. Owens, M. Pallis, Survivorship of meniscal allograft transplantation in an athletic patient population, Am. J. Sports Med. 44 (5) (2016) 1237–1242, https://doi.org/10.1177/0363546515626184.
[4] H.A. Kazi, W. Abdel-Rahman, P.A. Brady, J.C. Cameron, Meniscal allograft with or without osteotomy: a 15-year follow-up study, Knee Surg. Sports Traumatol. Arthrosc. 23 (1) (2015) 303–309, https://doi.org/10.1007/s00167-014-3291-z.
[5] R. Yan, Y. Chen, Y. Gu, C. Tang, J. Huang, Y. Hu, Z. Zheng, J. Ran, B. Heng, X. Chen, Z. Yin, W. Chen, W. Shen, H. Ouyang, A collagen-coated sponge silk scaffold for functional meniscus regeneration, J. Tissue Eng. Regen. Med. 13 (2) (2019) 156–173, https://doi.org/10.1002/term.2777.
[6] J. Baek, X. Chen, S. Sovani, S. Jin, S.P. Grogan, D.D. D'Lima, Meniscus tissue engineering using a novel combination of electrospun scaffolds and human meniscus cells embedded within an extracellular matrix hydrogel, J. Orthop. Res. : Off. Publ. Orthopaed. Res. Soc. 33 (4) (2015) 572–583, https://doi.org/10.1002/jor.22802.
[7] G. Zhong, J. Yao, X. Huang, Y. Luo, M. Wang, J. Han, F. Chen, Y. Yu, Injectable ECM hydrogel for delivery of BMSCs enabled full-thickness meniscus repair in an orthotopic rat model, BioactIVE Mater. 5 (4) (2020) 871–879, https://doi.org/10.1016/j.bioactmat.2020.06.008.
[8] Z.Z. Zhang, D. Jiang, J.X. Ding, S.J. Wang, L. Zhang, J.Y. Zhang, Y.S. Qi, X.S. Chen, J.K. Yu, Role of scaffold mean pore size in meniscus regeneration, Acta Biomater. 43 (2016) 314–326, https://doi.org/10.1016/j.actbio.2016.07.050.
[9] G. Bahcecioglu, G. Bahcecioglu, N. Hasirci, N. Hasirci, B. Bilgen, B. Bilgen, V. Hasirci, V. Hasirci, A 3D printed PCL/hydrogel construct with zone-specific biochemical composition mimicking that of the meniscus, Biofabrication 11 (2) (2019), 025002, https://doi.org/10.1088/1758-5090/aaf707.
[10] M.X. Chen, Z.X. Feng, W.M. Guo, D.J. Yan, S. Gao, Y.Y. Li, S. Shen, Z.G. Yuan, B. Huang, Y. Zhang, M.J. Wang, X. Li, L.B. Hao, J. Peng, S.Y. Liu, Y.X. Zhou, Q. Y. Guo, PCL-MECM-Based hydrogel hybrid scaffolds and meniscal fibrochondrocytes promote whole meniscus regeneration in a rabbit meniscectomy model, ACS Appl. Mater. Interfaces 11 (44) (2019) 41626–41639, https://doi.org/10.1021/acsami.9b13611.
[11] G. Bahcecioglu, B. Bilgen, N. Hasirci, V. Hasirci, Anatomical meniscus construct with zone specific biochemical composition and structural organization, Biomaterials 218 (2019) 119361, https://doi.org/10.1016/j.biomaterials.2019.119361.
[12] S. Gupta, A. Sharma, J. Vasantha Kumar, V. Sharma, P.K. Gupta, R.S. Verma, Meniscal tissue engineering via 3D printed PLA monolith with carbohydrate based self-healing interpenetrating network hydrogel, Int. J. Biol. Macromol. 162 (2020) 1358–1371, https://doi.org/10.1016/j.ijbiomac.2020.07.238.
[13] Y. Sun, Y. You, W. Jiang, Q. Wu, B. Wang, K. Dai, Generating ready-to-implant anisotropic menisci by 3D-bioprinting protein-releasing cell-laden hydrogel-polymer composite scaffold, Appl. Mater. Today 18 (2020) 100469, https://doi.org/10.1016/j.apmt.2019.100469.
[14] Z. Yuan, S. Liu, C. Hao, W. Guo, S. Gao, M. Wang, M. Chen, Z. Sun, Y. Xu, Y. Wang, J. Peng, M. Yuan, Q.Y. Guo, AMECM/DCB scaffold prompts successful total meniscus reconstruction in a rabbit total meniscectomy model, Biomaterials 111 (2016) 13–26, https://doi.org/10.1016/j.biomaterials.2016.09.017.
[15] J. Jang, H.J. Park, S.W. Kim, H. Kim, J.Y. Park, S.J. Na, H.J. Kim, M.N. Park, S. H. Choi, S.H. Park, S.W. Kim, S.M. Kwon, P.J. Kim, D.W. Cho, 3D printed complex tissue construct using stem cell-laden decellularized extracellular matrix bioinks for cardiac repair, Biomaterials 112 (2017) 264–274, https://doi.org/10.1016/j.biomaterials.2016.10.026.
[16] D.O. Freytes, J. Martin, S.S. Velankar, A.S. Lee, S.F. Badylak, Preparation and rheological characterization of a gel form of the porcine urinary bladder matrix, Biomaterials 29 (11) (2008) 1630–1637, https://doi.org/10.1016/j.biomaterials.2007.12.014.
[17] B.D. Fairbanks, M.P. Schwartz, C.N. Bowman, K.S. Anseth, Photoinitiated polymerization of PEG-diacrylate with lithium phenyl-2,4,6-trimethylbenzoylphosphinate: polymerization rate and cytocompatibility, Biomaterials 30 (35) (2009) 6702–6707, https://doi.org/10.1016/j.biomaterials.2009.08.055.
[18] M.S. Son, M.E. Levenston, Quantitative tracking of passage and 3D culture effects on chondrocyte and fibrochondrocyte gene expression, J Tissue Eng Regen Med 11 (4) (2017) 1185–1194, https://doi.org/10.1002/term.2022.
[19] G.A. Ballard, J.J. Warnock, G. Bobe, K.F. Duesterdieck-Zellmer, L. Baker, W. I. Baltzer, J. Ott, Comparison of meniscal fibrochondrocyte and synoviocyte bioscaffolds toward meniscal tissue engineering in the dog, Res. Vet. Sci. 97 (2) (2014) 400–408, https://doi.org/10.1016/j.rvsc.2014.05.002.
[20] A. Martin Seitz, F. Galbusera, C. Krais, A. Ignatius, L. Durselen, Stress-relaxation response of human menisci under confined compression conditions, J Mech Behav Biomed Mater 26 (2013) 68–80, https://doi.org/10.1016/j.jmbbm.2013.05.027.
[21] R.L. Spilker, P.S. Donzelli, V.C. Mow, A transversely isotropic biphasic finite element model of the meniscus, J. Biomech. 25 (9) (1992) 1027–1045, https://doi.org/10.1016/0021-9290(92)90038-3.
[22] Z.-Z. Zhang, S.-J. Wang, J.-Y. Zhang, W.-B. Jiang, A.-B. Huang, Y.-S. Qi, J.-X. Ding, X.-S. Chen, D. Jiang, J.-K. Yu, 3D-Printed poly(ε-caprolactone) scaffold augmented with mesenchymal stem cells for total meniscal substitution: a 12- and 24-week animal study in a rabbit model, Am. J. Sports Med. 45 (7) (2017) 1497–1511, https://doi.org/10.1177/0363546517691513.
[23] D. Jiang, L.H. Zhao, M. Tian, J.Y. Zhang, J.K. Yu, Meniscus transplantation using treated xenogeneic meniscal tissue: viability and chondroprotection study in rabbits, Arthroscopy 28 (8) (2012) 1147–1159, https://doi.org/10.1016/j.arthro.2012.01.001.

[24] R. Mohan, N. Mohan, D. Vaikkath, Hyaluronic acid dictates chondrocyte morphology and migration in composite gels, Tissue Eng. Part A 24 (19–20) (2018) 1481–1491, https://doi.org/10.1089/ten.TEA.2017.0411.
[25] F. Xu, F. Inci, O. Mullick, U.A. Gurkan, Y. Sung, D. Kavaz, B. Li, E.B. Denkbas, U. Demirci, Release of magnetic nanoparticles from cell-encapsulating biodegradable nanobiomaterials, ACS Nano 6 (8) (2012) 6640–6649, https://doi.org/10.1021/nn300902w.
[26] B. Rihova, Immunocompatibility and biocompatibility of cell delivery systems, Adv. Drug Deliv. Rev. 42 (1–2) (2000) 65–80, https://doi.org/10.1016/s0169-409x(00)00054-5.
[27] W. Liu, Y.S. Zhang, M.A. Heinrich, F. De Ferrari, H.L. Jang, S.M. Bakht, M. M. Alvarez, J. Yang, Y.C. Li, G. Trujillo-de Santiago, A.K. Miri, K. Zhu, P. Khoshakhlagh, G. Prakash, H. Cheng, X. Guan, Z. Zhong, J. Ju, G.H. Zhu, X. Jin, S. Ryon Shin, M.R. Dokmeci, A. Khademhosseini, Rapid continuous multimaterial extrusion bioprinting, Adv. Mater. 29 (3) (2017) 1604630, https://doi.org/10.1002/adma.201604630, n/a.
[28] N. Sears, P. Dhavalikar, M. Whitely, E. Cosgriff-Hernandez, Fabrication of biomimetic bone grafts with multi-material 3D printing, Biofabrication 9 (2) (2017), 025020, https://doi.org/10.1088/1758-5090/aa7077.
[29] A.L. Rutz, K.E. Hyland, A.E. Jakus, W.R. Burghardt, R.N. Shah, A multimaterial bioink method for 3D printing tunable, cell-compatible hydrogels, Adv. Mater. 27 (9) (2015) 1607–1614, https://doi.org/10.1002/adma.201405076.
[30] F. Pati, J. Jang, D.H. Ha, S. Won Kim, J.W. Rhie, J.H. Shim, D.H. Kim, D.W. Cho, Printing three-dimensional tissue analogues with decellularized extracellular matrix bioink, Nat. Commun. 5 (2014) 3935, https://doi.org/10.1038/ncomms4935.
[31] H.-W. Kang, S.J. Lee, I.K. Ko, C. Kengla, J.J. Yoo, A. Atala, A 3D bioprinting system to produce human-scale tissue constructs with structural integrity, Nat. Biotechnol. 34 (3) (2016) 312–319, https://doi.org/10.1038/nbt.3413.
[32] S.R. Moxon, N.J. Corbett, K. Fisher, G. Potjewyd, M. Domingos, N.M. Hooper, Blended alginate/collagen hydrogels promote neurogenesis and neuronal maturation, Mater. Sci. Eng. C 104 (2019) 109904, https://doi.org/10.1016/j.msec.2019.109904.
[33] J. Tavakoli, E. Laisak, M. Gao, Y. Tang, AIEgen quantitatively monitoring the release of Ca2+ during swelling and degradation process in alginate hydrogels, Mater. Sci. Eng. C 104 (2019) 109951, https://doi.org/10.1016/j.msec.2019.109951.
[34] Y.J. Seong, G. Lin, B.J. Kim, H.E. Kim, S. Kim, S.H. Jeong, Hyaluronic acid-based hybrid hydrogel microspheres with enhanced structural stability and high injectability, ACS Omega 4 (9) (2019) 13834–13844, https://doi.org/10.1021/acsomega.9b01475.
[35] M. Li, X. Zhang, W. Jia, C. Wang, X. Wang, Q. Wang, Y. Liu, J. Jiang, G. Gu, Z. Guo, Z. Chen, Improving in vitro biocompatibility on biomimetic mineralized collagen bone materials modified with hyaluronic acid oligosaccharide, Mater. Sci. Eng. C 104 (2019) 110008, https://doi.org/10.1016/j.msec.2019.110008.
[36] J.H. Kim, I. Kim, Y.J. Seol, I.K. Ko, J.J. Yoo, A. Atala, S.J. Lee, Neural cell integration into 3D bioprinted skeletal muscle constructs accelerates restoration of muscle function, Nat. Commun. 11 (1) (2020) 1025, https://doi.org/10.1038/s41467-020-14930-9.
[37] D. Kang, G. Hong, S. An, I. Jang, W.S. Yun, J.H. Shim, S. Jin, Bioprinting of multiscaled hepatic lobules within a highly vascularized construct, Small 16 (13) (2020), e1905505, https://doi.org/10.1002/smll.201905505.
[38] A. Lee, A.R. Hudson, D.J. Shiwarski, J.W. Tashman, T.J. Hinton, S. Yerneni, J. M. Bliley, P.G. Campbell, A.W. Feinberg, 3D bioprinting of collagen to rebuild components of the human heart, Science 365 (6452) (2019) 482–487, https://doi.org/10.1126/science.aav9051.
[39] E. Garreta, R. Oria, C. Tarantino, M. Pla-Roca, P. Prado, F. Fernández-Avilés, J. M. Campistol, J. Samitier, N. Montserrat, Tissue engineering by decellularization and 3D bioprinting, Mater. Today 20 (4) (2017) 166–178, https://doi.org/10.1016/j.mattod.2016.12.005.
[40] D. Chimene, K.K. Lennox, R.R. Kaunas, A.K. Gaharwar, Advanced bioinks for 3D printing: a materials science perspective, Ann. Biomed. Eng. 44 (6) (2016) 2090–2102, https://doi.org/10.1007/s10439-016-1638-y.
[41] H. Lin, G. Yang, J. Tan, R.S. Tuan, Influence of decellularized matrix derived from human mesenchymal stem cells on their proliferation, migration and multi-lineage differentiation potential, Biomaterials 33 (18) (2012) 4480–4489, https://doi.org/10.1016/j.biomaterials.2012.03.012.
[42] K.A. Garvin, J. VanderBurgh, D.C. Hocking, D. Dalecki, Controlling collagen fiber microstructure in three-dimensional hydrogels using ultrasound, J. Acoust. Soc. Am. 134 (2) (2013) 1491–1502, https://doi.org/10.1121/1.4812868.
[43] B.J. Klotz, D. Gawlitta, A. Rosenberg, J. Malda, F.P.W. Melchels, Gelatin-methacryloyl hydrogels: towards biofabrication-based tissue repair, Trends Biotechnol. 34 (5) (2016) 394–407, https://doi.org/10.1016/j.tibtech.2016.01.002.
[44] H. Aubin, J.W. Nichol, C.B. Hutson, H. Bae, A.L. Sieminski, D.M. Cropek, P. Akhyari, A. Khademhosseini, Directed 3D cell alignment and elongation in microengineered hydrogels, Biomaterials 31 (27) (2010) 6941–6951, https://doi.org/10.1016/j.biomaterials.2010.05.056.
[45] O. Chaudhuri, J. Cooper-White, P.A. Janmey, D.J. Mooney, V.B. Shenoy, Effects of extracellular matrix viscoelasticity on cellular behaviour, Nature 584 (7822) (2020) 535–546, https://doi.org/10.1038/s41586-020-2612-2.
[46] A.J. Rufaihah, S. Cheyyatraivendran, M.D.M. Mazlan, K. Lim, M.S.K. Chong, C.N. Z. Mattar, J.K.Y. Chan, T. Kofidis, D. Seliktar, The effect of scaffold modulus on the morphology and remodeling of fetal mesenchymal stem cells, Front. Physiol. 9 (2018) 1555, https://doi.org/10.3389/fphys.2018.01555.
[47] A.C. Daly, S.E. Critchley, E.M. Rencsok, D.J. Kelly, A comparison of different bioinks for 3D bioprinting of fibrocartilage and hyaline cartilage, Biofabrication 8 (4) (2016), 045002.
[48] W. Shang, Y. Liu, W. Wan, C. Hu, Z. Liu, C.T. Wong, T. Fukuda, Y. Shen, Hybrid 3D printing and electrodeposition approach for controllable 3D alginate hydrogel formation, Biofabrication 9 (2) (2017), 025032, https://doi.org/10.1088/1758-5090/aa6ed8.
[49] S. Xiao, T. Zhao, J. Wang, C. Wang, J. Du, L. Ying, J. Lin, C. Zhang, W. Hu, L. Wang, K. Xu, Gelatin methacrylate (GelMA)-Based hydrogels for cell transplantation: an effective strategy for tissue engineering, Stem Cell Rev. Rep. 15 (5) (2019) 664–679, https://doi.org/10.1007/s12015-019-09893-4.
[50] J. Yin, M. Yan, Y. Wang, J. Fu, H. Suo, 3D bioprinting of low-concentration cell-laden gelatin methacrylate (GelMA) bioinks with a two-step cross-linking strategy, ACS Appl. Mater. Interfaces 10 (8) (2018) 6849–6857, https://doi.org/10.1021/acsami.7b16059.
[51] A.C. Daly, S.E. Critchley, E.M. Rencsok, D.J. Kelly, A comparison of different bioinks for 3D bioprinting of fibrocartilage and hyaline cartilage, Biofabrication 8 (4) (2016), 045002, https://doi.org/10.1088/1758-5090/8/4/045002.
[52] Y. Zhao, Y. Li, S. Mao, W. Sun, R. Yao, The influence of printing parameters on cell survival rate and printability in microextrusion-based 3D cell printing technology, Biofabrication 7 (4) (2015), 045002, https://doi.org/10.1088/1758-5090/7/4/045002.
[53] J. Kundu, J.H. Shim, J. Jang, S.W. Kim, D.W. Cho, An additive manufacturing-based PCL–alginate–chondrocyte bioprinted scaffold for cartilage tissue engineering, J. Tissue Eng. Regen. Med. 9 (11) (2015) 1286–1297, https://doi.org/10.1002/term.1682.
[54] S. Romanazzo, S. Vedicherla, C. Moran, D.J. Kelly, Meniscus ECM-functionalised hydrogels containing infrapatellar fat pad-derived stem cells for bioprinting of regionally defined meniscal tissue, J. Tissue Eng. Regen. Med. 12 (3) (2018) e1826–e1835, https://doi.org/10.1002/term.2602.
[55] F. Pati, D.H. Ha, J. Jang, H.H. Han, J.W. Rhie, D.W. Cho, Biomimetic 3D tissue printing for soft tissue regeneration, Biomaterials 62 (2015) 164–175, https://doi.org/10.1016/j.biomaterials.2015.05.043.
[56] A. Bandyopadhyay, B.B. Mandal, A three-dimensional printed silk-based biomimetic tri-layered meniscus for potential patient-specific implantation, Biofabrication 12 (1) (2019), 015003, https://doi.org/10.1088/1758-5090/ab40fa.
[57] H.N. Chia, M.L. Hull, Compressive moduli of the human medial meniscus in the axial and radial directions at equilibrium and at a physiological strain rate, J. Orthop. Res. 26 (7) (2008) 951–956, https://doi.org/10.1002/jor.20573.
[58] K.M. Fischenich, K. Boncella, J.T. Lewis, T.S. Bailey, T.L. Haut Donahue, Dynamic compression of human and ovine meniscal tissue compared with a potential thermoplastic elastomer hydrogel replacement: dynamic compression OF human and ovine meniscal tissue, J. Biomed. Mater. Res. 105 (10) (2017) 2722–2728, https://doi.org/10.1002/jbm.a.36129.
[59] M. Tissakht, A.M. Ahmed, Tensile stress-strain characteristics of the human meniscal material, J. Biomech. 28 (4) (1995) 411–422, https://doi.org/10.1016/0021-9290(94)00081-E.
[60] D.W. Hutmacher, Scaffolds in tissue engineering bone and cartilage, Biomaterials 21 (24) (2000) 2529–2543, https://doi.org/10.1016/S0142-9612(00)00121-6.
[61] Y. Zhu, Y. Zhu, T. Liu, T. Liu, K. Song, K. Song, B. Jiang, B. Jiang, X. Ma, X. Ma, Z. Cui, Z. Cui, Collagen–chitosan polymer as a scaffold for the proliferation of human adipose tissue-derived stem cells, J. Mater. Sci. Mater. Med. 20 (3) (2009) 799–808, https://doi.org/10.1007/s10856-008-3636-6.
[62] P. Jithendra, A.M. Rajam, T. Kalaivani, A.B. Mandal, C. Rose, Preparation and characterization of aloe vera blended collagen-chitosan composite scaffold for tissue engineering applications, ACS Appl. Mater. Interfaces 5 (15) (2013) 7291–7298, https://doi.org/10.1021/am401637c.
[63] C.X.F. Lam, D.W. Hutmacher, J.T. Schantz, M.A. Woodruff, S.H. Teoh, Evaluation of polycaprolactone scaffold degradation for 6 months in vitro and in vivo, J. Biomed. Mater. Res. 90A (3) (2009) 906–919, https://doi.org/10.1002/jbm.a.32052.
[64] C.X.F. Lam, M.M. Savalani, S.-H. Teoh, D.W. Hutmacher, Dynamics of in vitro polymer degradation of polycaprolactone-based scaffolds: accelerated versus simulated physiological conditions, Biomed. Mater. 3 (3) (2008), 034108, https://doi.org/10.1088/1748-6041/3/3/034108.
[65] A.R. Hernández, O.C. Contreras, J.C. Acevedo, L.G.N. Moreno, Poly (ε-caprolactone) degradation under acidic and alkaline conditions, Am. J. Polym. Sci. 3 (2013) 70–75.
[66] A.M. Martins, Q.P. Pham, P.B. Malafaya, R.A. Sousa, M.E. Gomes, R.M. Raphael, F. K. Kasper, R.L. Reis, A.G. Mikos, The role of lipase and α-amylase in the degradation of starch/poly(Caprolactone) fiber meshes and the osteogenic differentiation of cultured marrow stromal cells, Tissue Eng. 15 (2) (2009) 295–305, https://doi.org/10.1089/ten.tea.2008.0025.
[67] J.N. Hoskins, S.M. Grayson, Synthesis and degradation behavior of cyclic poly (ε-caprolactone), Macromolecules 42 (17) (2009) 6406–6413, https://doi.org/10.1021/ma9011076.
[68] Y. Zhang, F. Rossi, S. Papa, M.B. Violatto, P. Bigini, M. Sorbona, F. Redaelli, P. Veglianese, J. Hilborn, D.A. Ossipov, v. Teknisk-naturvetenskapliga, Polymerkemi, Å. Institutionen för kemi, U. Uppsala, S. Kemiska, Non-invasive in vitro and in vivo monitoring of degradation of fluorescently labeled hyaluronan hydrogels for tissue engineering applications, Acta Biomater. 30 (2016) 188–198, https://doi.org/10.1016/j.actbio.2015.11.053.
[69] X. Ma, X. Sun, D. Hargrove, J. Chen, D. Song, Q. Dong, X. Lu, T.-H. Fan, Y. Fu, Y. Lei, A biocompatible and biodegradable protein hydrogel with green and red autofluorescence: preparation, characterization and in vivo biodegradation

tracking and modeling, Sci. Rep. 6 (1) (2016) 19370, https://doi.org/10.1038/srep19370.

[70] X. Dong, C. Wei, T. Liu, F. Lv, Z. Qian, Real-time fluorescence tracking of protoporphyrin incorporated thermosensitive hydrogel and its drug release in vivo, ACS Appl. Mater. Interfaces 8 (8) (2016) 5104–5113, https://doi.org/10.1021/acsami.5b11493.

[71] P.N. Oliveira, A. Montembault, G. Sudre, P. Alcouffe, L. Marcon, H. Gehan, F. Lux, K. Albespy, V. Centis, D. Campos, S. Roques, M. Meulle, M. Renard, M. Durand, Q. Denost, L. Bordenave, M. Vandamme, E. Chereul, M. Vandesteene, N. Boucard, L. David, Self-crosslinked fibrous collagen/chitosan blends: processing, properties evaluation and monitoring of degradation by bi-fluorescence imaging, Int. J. Biol. Macromol. 131 (2019) 353–367, https://doi.org/10.1016/j.ijbiomac.2019.02.134.

[72] R. Mueller-Rath, K. Gavénis, S. Gravius, S. Andereya, T. Mumme, U. Schneider, In vivo cultivation of human articular chondrocytes in a nude mouse-based contained defect organ culture model, Bio Med. Mater. Eng. 17 (6) (2007) 357–366.